Acta Materialia 274 (2024) 119990

Contents lists available at ScienceDirect

Acta Materialia

journal homepage: www.elsevier.com/locate/actamat

Full length article

Origins of functional fatigue and reversible transformation of precipitates in NiTi shape memory alloy

R. Sidharth, T.B. Celebi, H. Sehitoglu *

Department of Mechanical Science and Engineering, University of Illinois at Urbana-Champaign, 1206W. Green St., Urbana, IL 61801, USA

ARTICLE INFO

Keywords:
In situ-TEM
Martensitic transformation
R phase
Shape memory alloys
Dislocations

ABSTRACT

The work clarifies several key questions in shape memory research that have eluded previous studies. The findings show that dislocation slip emanates at austenite-martensite interfaces during unloading and aligns with the internal twin boundary interface of martensite. It was observed that the type II internal twins of the martensite become parallel dislocations in the austenite. During reloading, these dislocations act as nucleation sites for the martensitic twins, reducing the nucleation barrier and the transformation stress. The precipitates facilitate martensite nucleation but also act as an obstacle to martensite front motion, restrict detwinning, and pin the interfacial dislocations during unloading, thereby contributing to residual strains and martensite stabilization. Martensite nucleation is not suppressed by the size of the thin film, which is of the order of 85 to 105 nanometers thick, and repeated transformation occurred cycle after cycle. Single crystals deformed in the <101>$_{LD}$ exhibited the best recoverability of up to 5.5 % and tensile stresses of up to 1.4 GPa. It was demonstrated for the first time that, when favorably oriented, Ni_4Ti_3 precipitates undergo a reversible phase transformation to R-phase and can accommodate up to 4 % reversible strains.

1. Introduction

The reversible martensitic transformation has been of interest to the scientific community for more than half a century [1,2]. Asserting a ubiquitous presence in nature, martensitic transformations are not only observed in metallic and ceramic systems but also in biological systems such as bacteria and viruses aiding in performing life functions [3]. Shape memory alloys (SMA) are one such class of metallic systems which, upon the application of stress, undergo an austenitic to martensitic phase transformation, resulting in large strain accommodation. Reversal of this phase transformation by unloading (superelastic effect) or unloading followed by heating (shape memory effect) recovers almost all the strain. NiTi, technologically the most important shape memory alloy of today, is being used in engineering applications like biomedical stents, solid state actuators, active/passive damping, and elastocaloric cooling, to name a few [4–10]. Barring the extensive applications of SMAs in the macro-scale, there is immense interest in employing SMAs in the small length scales such as in micro-stents, micro-valves, micro-pumps, actuators in micro-electromechanical and nano-electromechanical systems (MEMS/NEMS), and biomimetic systems [11–20]. Therefore, it is imperative to study the nanomechanical properties of NiTi, especially in tensile fatigue.

Functional characteristics of NiTi, like transformation stress, hysteresis, strain recovery, and elastocaloric capacity, deteriorate upon fatigue. By comparing between two bulk single crystals of $Ni_{50.8}Ti$ compressed along the $\langle 011 \rangle$ and $\langle 001 \rangle$ loading axis [21], we had previously demonstrated that the root cause for all such declension could be linked to the accumulation of transformation-induced defects like dislocations and residual martensite. There is a wealth of information in the literature regarding the mechanisms behind functional degradation. Experiments [22–32] and modeling efforts [27,29,33–35] have explicitly shown the role played by the A-M interface and the internal twin interfaces of the martensite in transformation-induced defects in diverse SMAs. Furthermore, transformation-induced defects act as precursors to structural failure in diverse SMAs like FeMnAlNi [36,37], NiTi [38], and CuZnAl [36–38]. Despite such extensive experimental and modeling efforts, some important questions still need to be answered. When and where are these defects generated? How do they interact with the transformation front in the subsequent cycles and modify the functional characteristics? In addition to that, post-mortem TEM analysis in our previous work showed that the Ni_4Ti_3 nano-precipitates underwent deformation and contributed to the functional fatigue [21]. This

---

* Corresponding author.
E-mail address: huseyin@illinois.edu (H. Sehitoglu).

https://doi.org/10.1016/j.actamat.2024.119990
Received 28 January 2024; Received in revised form 6 May 2024; Accepted 7 May 2024

prompts one to explore the mechanisms behind such observations and suspect whether precipitates might exhibit superelasticity. Historically, it has been assumed that precipitates do not transform in NiTi [39].

To answer such inquisitions, direct observation of stress-induced martensitic transformation in the presence of nano-precipitates and transformation induced defect generation in the nanoscale volumes is needed. *In situ* deformation experiment in the TEM is ideal as it offers diffraction contrast imaging, thus enabling direct observation of the dynamic aspects of martensite evolution, its interaction with transformation-induced defects, and the role played by Ni_4Ti_3 nano-precipitates. Understanding the microstructural mechanisms behind these events would further the knowledge of fatigue irreversibility in SMAs, enabling the development of accurate models faithful to the underlying physics, especially in the nanoscale, and facilitate physically informed design optimization of nano-machines. Superelasticity in the micro to nano scale has been primarily tested by pillar compression tests with pillar diameters ranging from 2 μm to 200 nm [27,29,35,40–45]. On the contrary, probing superelastic deformation mechanisms in nanoscale tensile samples offers many advantages. Due to the propensity of buckling, the diameter of the nano-compression pillar needs to be rather large, limiting sample transparency and hindering precise observation of the martensitic transformation mechanisms; this can be circumvented in nano-tensile samples. There have been few studies that report *in situ* TEM observations of martensitic transformation in NiTi under tensile straining [30,46–50]. However, these studies do not report the recovery of martensite upon unloading nor the pertinent mechanisms; hence, there is no way of knowing if superelastic reversibility was achieved. In a recent study by the current authors, superelasticity was demonstrated in nano-tension while observing the fatigue failure mechanisms in nanoscale thin film NiTi [51] with unprecedented clarity.

Following suit, in this study, systematic evaluation of nanoscale superelasticity and the mechanisms giving rise to functional fatigue was undertaken by loading electron transparent nano-tensile samples along $\langle 111\rangle$, $\langle 011\rangle$, and $\langle 121\rangle$ loading orientations for multiple cycles. Choosing different loading orientations offers an opportunity to sample different precipitate variants that have $\{111\}_{B2}$habit planes with longitudinal axes along $<101>_{B2}$ directions. Thus, the role played by different precipitate variants can be observed. In addition, the different viewing directions of these samples offer the ability to view martensite, its internal substructure, and the pertinent defects under different diffraction contrast conditions, allowing for accurate deduction of the mechanisms at play. In summary, in this study, we first demonstrate superelasticity in free-standing NiTi thin films pulled along different loading orientations. Then, we break down the complexity of functional fatigue irreversibility in the nanoscale by directly observing the mechanisms in real-time with unprecedented clarity. Finally, we show for the first time that, if the precipitates are favorably oriented, they indeed undergo a reversible phase transformation exhibiting superelasticiy for over 20 cycles and accommodate up to 4 % recoverable strain.

2. Experimental techniques

2.1. Material and heat treatment

$Ni_{50.8}Ti$ (at%) single crystals were grown using the Bridgeman technique in an inert environment. Single crystal ingots were solutionized at 920 °C for 24 h in argon, then water quenched. Miniature blocks of $4 \times 4 \times 8\ mm^3$ dimension were EDM cut out of the ingot, aged at 550 °C for 1.5 h, and water quenched to produce coherent, homogenous lenticular Ni_4Ti_3 precipitates in the matrix [25]. The transformation temperatures obtained via differential scanning calorimetry (DSC) (Fig. 1b) are as follows: $A_s = -18\ ^\circ C$, $A_f = 1\ ^\circ C$, $M_s = -55\ ^\circ C$ and $M_f = -70\ ^\circ C$. This heat treatment results in a single-step B2 to B19' phase transformation, and the sample was fully austenitic at room temperature, thereby exhibiting superelastic behavior.

2.2. Sample preparation

The EDM cut blocks were sequentially polished all the way from P400 SiC abrasive paper down to 0.02 μm colloidal silica to achieve a satisfactory surface finish for backscattered electron diffraction (EBSD). The crystallographic orientation of the blocks was identified as [101], $[1\bar{3}\bar{1}]$ and $[\bar{2}12]$ (Fig. 1b). Then, 20 μm long and 1 μm thick FIB lift-out samples were extracted from the [101] plane with $[11\bar{1}]$, $[\bar{1}21]$, $[0\bar{1}0]$ foil normal corresponding to $[\bar{1}21]$, $[11\bar{1}]$and $[10\bar{1}]$ loading directions respectively (Fig. 1b). These samples were initially attached to the conventional 4-post TEM copper grid and thinned down to 800 nm thickness at 30 kV and 0.43 nA probe current. On the other hand, the push-to-pull device, which comes with a standard 2.5 μm gage length, was milled to increase the gap to 7 μm. A rectangular $8 \times 2 \times 2\ \mu m^3$ platinum layer was deposited on either side of this gap and then milled

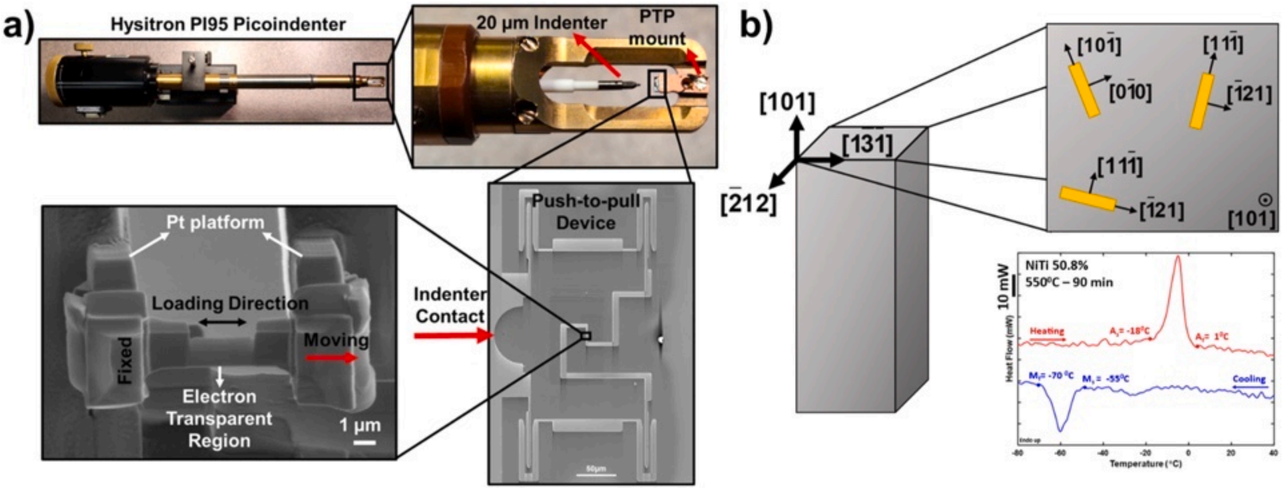

Fig. 1. a) Experimental setup which includes the Hysitron PI95 Picoindenter equipped with a 20 μm conductive flat punch conical diamond indenter and the push-to-pull device housing the electron transparent sample. Samples with different viewing directions and loading directions as shown in b) were lifted out of the bulk single crystal via FIB milling. Samples were pre-thinned to 800 nm on a conventional TEM grid, then transferred to the PTP device, where it was thinned down to a final thickness of about 100 nm. A representative electron transparent sample is shown in a). The width of the gage section ranged from 1.2 μm to 1.6 μm, length from 2.8 μm to 3 μm and thickness around 85 to 105 nm. The transformation temperatures measured via differential scanning calorimetry (DSC) is also shown in b).

to create a $6^\circ-7^\circ$ ramp. This facilitates elevation and pre-tilting of the micro-tensile sample with respect to the PTP surface to achieve edge-on condition for final thinning. This procedure is similar to what is described in [51,52]. The lift-out sample was removed from the TEM grid and transferred onto the platinum platform on the PTP using the Autoprobe™ micro-manipulator needle and attached by depositing more platinum. The stage, which has the PTP with the ramped-platinum platform, was tilted $6^\circ-7^\circ$ before attaching the sample. This ensures that the sample edge and the edge of the ramp are parallel. Now, during final thinning, the entire gage length of the sample (≈7 μm) was thinned down from 800 nm to about 400 nm at 30 kV, 0.23 nA probe current. Then, the central region of the sample, about 3 μm in length, was thinned from 400 nm to about 100 nm at 30 kV, 80 pA probe current. During these thinning stages, the sample was tilted ± 2° off the edge-on condition to thin the front and back sides, respectively. Finally, at 5 kV, 48 pA probe current, the sample was tilted ± 5° from the edge-on condition for polishing/cleaning to remove ion damage and create a smooth gage section with little to no defects, ideal for nanomechanical fatigue testing and simultaneous high-quality imaging in the TEM.

2.3. *In situ TEM tensile testing*

As shown in Fig. 1a, Hysitron PI95 Picoindenter was used for the nanomechanical test. The Picoindenter is equipped with a 60° conical, flat punch conductive diamond indenter with a 20 μm diameter. The diamond indenter was first coarse aligned with the PTP under an optical microscope. Then, *in situ* tensile test was performed in a JOEL 2010 LaB$_6$ TEM operating at 200 kV accelerating voltage. The Picoindenter can only be tilted about the x-axis, thereby hindering the attainment of perfect on-zone viewing condition. However, extracting the lamella as shown in Fig. 1b, ensured that the foil normal was as close as possible to the desired zone axis. Once the sample was tilted to achieve the appropriate diffraction and contrast condition, the diamond indenter was fine-aligned with the PTP inside the TEM. The samples were loaded under displacement control at the rate of 3–5 nm/s resulting in a strain rate of 5×10^{-4} to 1.3×10^{-3} s^{-1}. The engineering strain was calculated by manually measuring the displacement of microstructural markers in the sample such as the edge of electron transparent gage section as shown in Fig. 2b (dotted arrows), and the engineering stress was calculated from the measured load. PTP stiffness, measured after the failure of each sample, ranged from 400 to 500 N/m, close to the manufacturer's specification of 450 N/m. The load carried by the PTP was subtracted from the total load to obtain the load carried by the micro-tensile sample. Due to the inherent variations in the sample preparation procedure, it should be noted that the sample thickness/width may vary across the gage length. Thickness contrast can be observed in the *in situ* videos. Therefore, the reported values are average values for the whole gage length of the sample. Videos were captured during *in situ* loading at 1fps, 4000×2600 pixel^2 resolution using the Gatan SC1000 CCD camera. Transformation stress was obtained by extracting the timestep at the onset of transformation from the video and aligning it with the load vs. time plots. Defects like dislocations and residual martensite were distinguished by tilting the sample to leverage diffraction contrast from these defects (see appendix). As the picoindenter can only be tilted about the x-axis, all the diffraction conditions were not accessible.

3. Experimental results

3.1. ***NiTi $[\bar{1}21]_{LD}$ and $[11\bar{1}]$zone axis***

The stress displacement curve for cycle 1 is shown in Fig. 2 (supplementary video 1). Before loading, the initial microstructure (Fig. 2b) was purely austenitic, devoid of martensite or dislocations. As shown in Fig. 2a inset, the volume fraction of precipitate variant 1 was around 15 %, variant 2 was around 1.4 %, and variant 3 was around 1.6 %. The sample was loaded in displacement control, and Fig. 2a depicts the stress-displacement curve. As the stress level reaches around 480 MPa, martensite nucleated from precipitate variant 1. Martensite has a needle-like morphology and grows longitudinally. As the applied displacement is increased, multiple martensite needles nucleate and coalesce, as shown in Fig. 2d. These regions begin to detwin at a stress level of 640 MPa and 4.07 % applied strain. Detwinning accommodates about 1.13 % strain. One can note that detwinning occurs inhomogeneously, occurring only in regions where high density of martensite needles have coalesced. On the microstructural level, these regions are local stress hotspots such as near precipitates, as shown by the red arrows in Fig. 2e. As detwinning proceeds, the stress levels initially decrease, indicating intrinsic softening. However, the stress begins to rise again due to constraint from the surrounding microstructure. During the unloading stage, most of the martensite needles recede longitudinally along the same path and recover completely. However, detwinned regions do not recover (see supplementary video 1). During cycle 2 and cycle 3, regions enclosed in the red box in Fig. 2g were observed in real-time to uncover the mechanisms of martensite nucleation during fatigue loading.

The snapshots taken during cycle 2 are shown in Fig. 3 (supplementary video 2). Dislocation loops are discernable ahead of the residual martensite needle in Fig. 3b. As the load increases, the residual martensite proceeds to detwin. Detwinning is facilitated by the motion of twin partials [53], which consequently facilitates the movement of the austenite-martensite interface, resulting in the widening of the residual martensite domain, as seen in Fig. 3c. Dislocation loops act as nucleation points for martensite, resulting in a drop in transformation stress from 480 MPa in cycle 1 to 392 MPa in cycle 2, possibly due to the reduction in the martensite nucleation barrier. Once the stress reaches 475 MPa, martensite nucleates from the residual martensite-austenite interface (Fig. 3d). The interfacial dislocations act as nucleation points for fresh martensite needles. During the nucleation stage, each martensite needle's width is about 5 - 10 nm and grows to about 25 nm in width at maximum applied displacement. Martensite needles ahead of the tip of the residual martensite domain coalesce (Fig. 3d) and detwin (Fig. 3e). Finally, upon unloading, these martensite needles recede along the same path back to their point of nucleation (Fig. 3f), leaving behind dislocation loops ahead of the residual martensite tip (Fig. 3g) and interfacial dislocations along the residual martensite interface, which pins the interface and gives rise to unrecovered strains. Cycle after cycle, the residual martensite domains grow wider and longer by this mechanism.

Fig. 4 shows the snapshots taken during cycle 3 loading and unloading (supplementary video 3). The internally twinned residual martensite is perceptible in Fig. 4b. At a stress of 340 MPa (Fig. 4c) martensite needles nucleate from the dislocation loops and interfacial dislocations and extend into the B2 matrix. As loading proceeds, the detwinning of the residual martensite domain is perceptible in Fig. 4d. A different martensite variant nucleated from the tip of precipitate variant 1 as shown by the red arrow in Fig. 4d. At the maximum load, almost all of the B2 matrix in the field of view has completely transformed to martensite, coalesced martensite needles detwinned in some regions and at least 2 martensitic variants were present. Loading was paused to take a diffraction pattern (inset Fig. 4f) which reveals a type I twin relationship between the two variants which is the common junction plane between habit plane variants in a self-accommodating martensitic microstructure that clusters around $[111]_{B2}$ pole [54]. Unfortunately, probably due to mechanical instability, the sample catastrophically failed outside the field of view at an applied displacement of 143 nm. When investigating the post-fracture microstructure (Fig. 4f), new dislocation loops can be found in the matrix, and the residual martensite domain has visibly widened. After carefully observing the microstructure by tilting, the evolution of interfacial dislocations after 3 applied cycles can be clearly discerned in Fig. 5. Interfacial dislocation segments

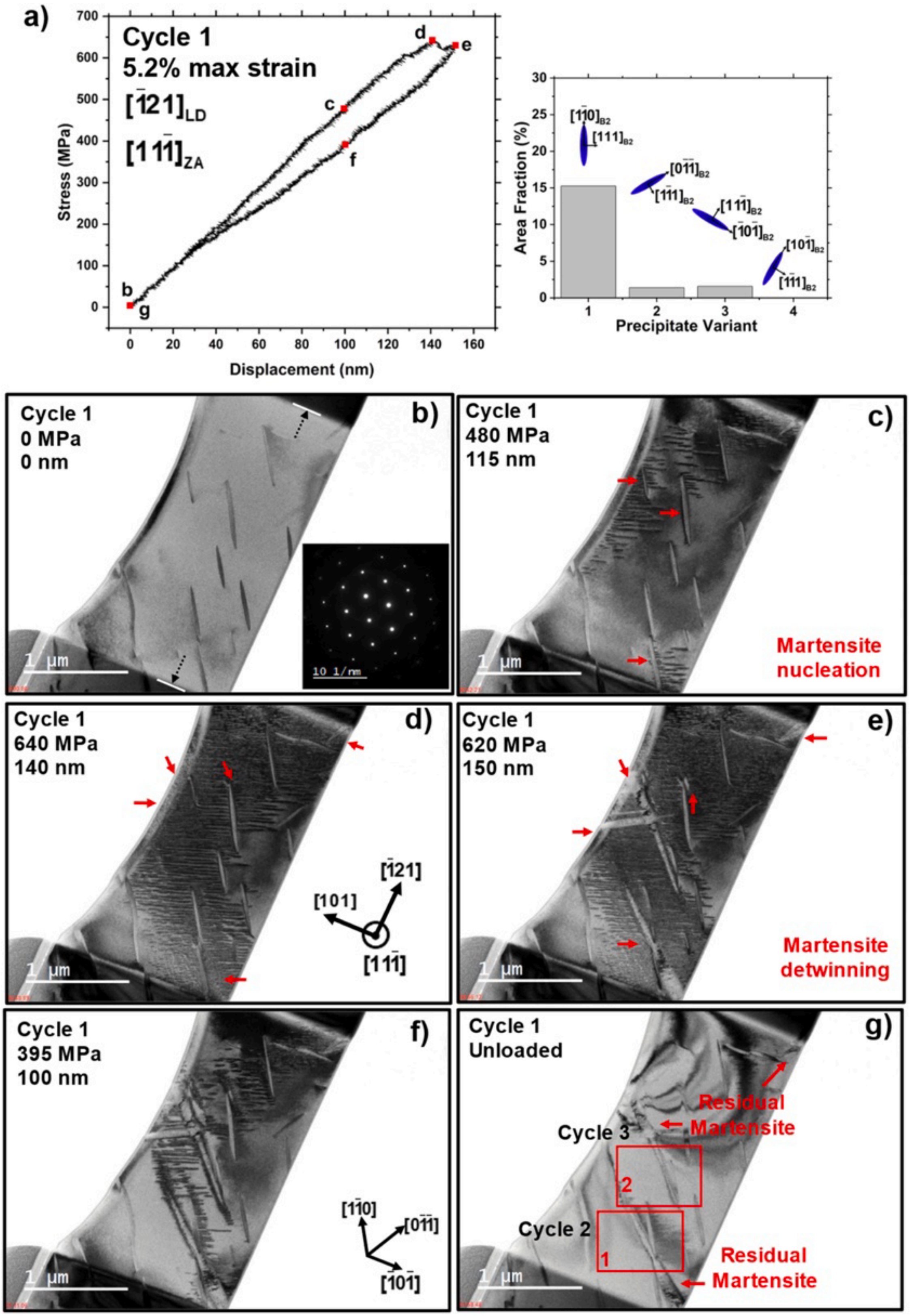

Fig. 2. a) Stress vs Displacement curve. Inset features the volume fraction of different precipitate variants. Stress drops as martensite undergoes detwinning. b) Austenite microstructure before loading. The strains were calculated by tracking the edge of the electron transparent gage section (dotted arrows). Note that the microstructure is devoid of any dislocations or martensite. c) Martensite nucleates from precipitates. d) Martensite coalescence can be observed in regions marked by red arrows. The high density of internal twins can be observed. Detwinning commences in these regions. e) Local detwinning accommodates 1.13 % strain and results in intrinsic softening. f) During unloading, martensite needles revert along the same path, back to the point of nucleation. g) After unloading, the detwinned martensite does not recover, giving rise to permanent strains. See supplementary video 1.

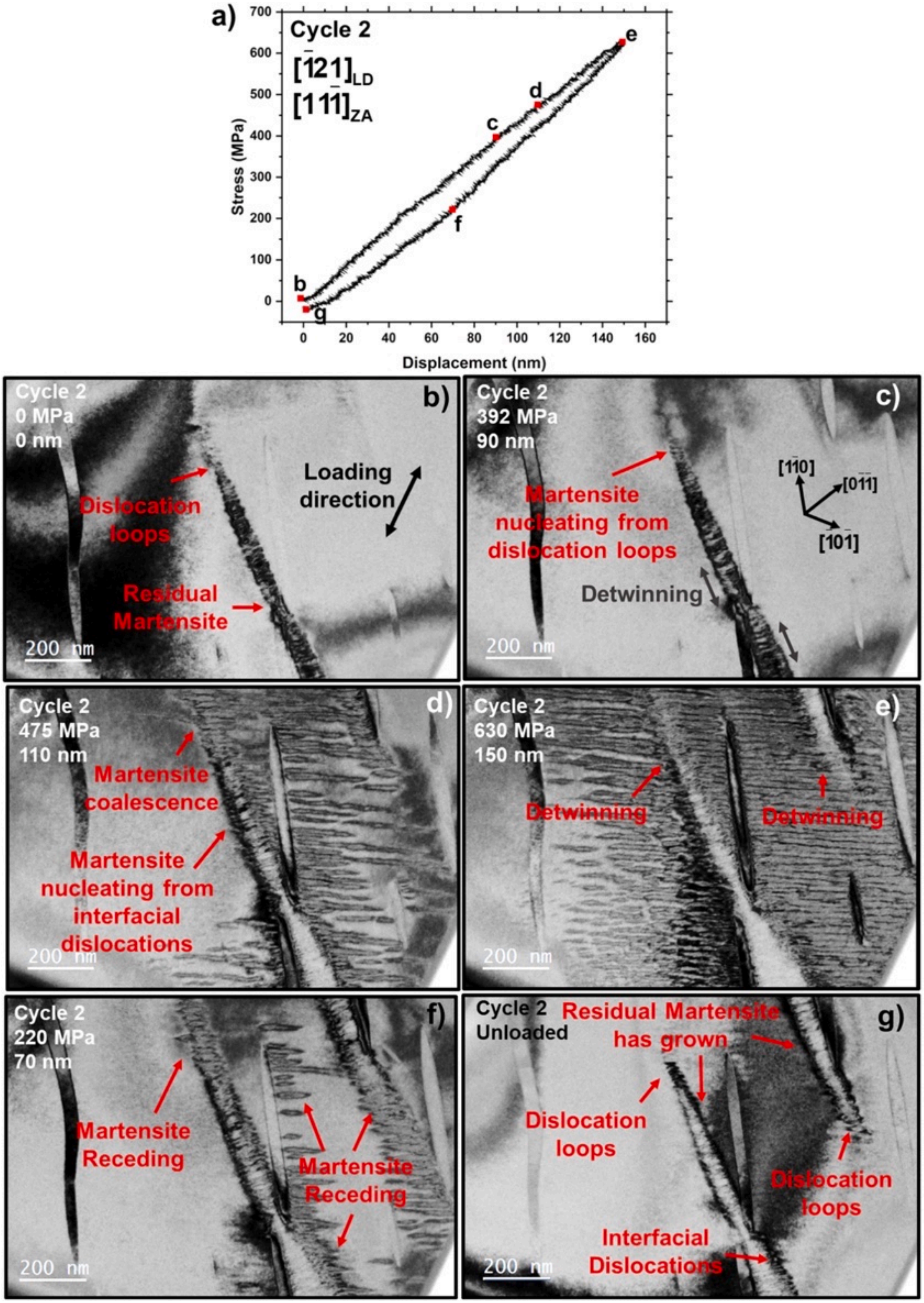

Fig. 3. *In situ*, TEM snapshots were taken during cycle 2 loading and unloading. a) Stress displacement curve for cycle 2. b) Before loading, dislocation loops ahead of the residual martensite can be seen. c) Residual martensite detwins during elastic loading and stress-induced martensite first nucleates from the dislocation loops at a stress level of 392 MPa. d) At a higher stress level of 475 MPa martensite nucleates from interfacial dislocations and martensite needles coalesce near the tip of residual martensite domains. e) At the maximum applied displacement, detwinning of freshly coalesced martensite needles is clear. f) During unloading, martensite needles disaggregate and recede along the same path. g) This leaves behind dislocation loops, tiny embryo of martensite (≈ 25 nm x 5 nm) ahead of the residual martensite tips, and interfacial dislocations along the martensite-austenite interface, thereby contributing to the accumulation of permanent strain. See supplementary video 2.

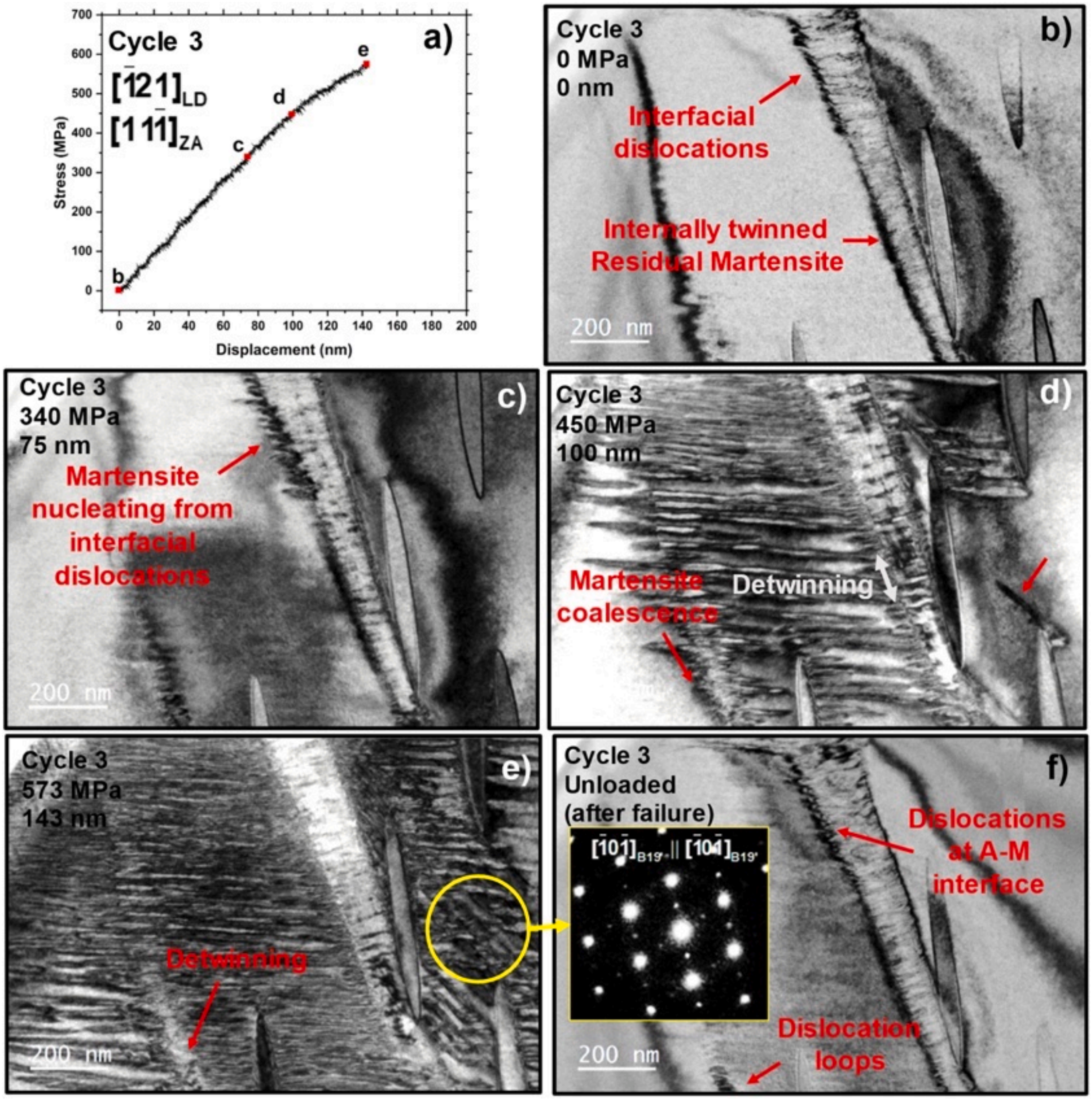

Fig. 4. TEM snapshots taken during cycle 3. b) Internally twinned residual martensite is visible in the microstructure before loading. c) Martensite needles nucleate from interfacial dislocations at a stress value of 340 MPa. d) Residual Martensite detwins as the applied displacement is increased and the individual martensite needles coalesce. A new martensite variant is observed to nucleate from tip of precipitate variant 1 (red arrow). e) Both martensite variants seem to intersect, and the diffraction pattern reveals a type I twin relationship which is the junction plane between habit plane variants in a self-accommodating martensitic structure [54]. Martensite detwinning is also evident. f) After unloading (i.e. fracture), dislocation loops are left behind, and the residual martensite has widened. See supplementary video 3.

appear elongated after 3 loading cycles and seem to be a direct extension of the internal twins of the martensite. The diffraction pattern reveals a type II twinning relationship and the trace of the B2 slip plane is nearly parallel to the trace of martensite twinning plane.

This is direct evidence that the transformation induced dislocations stem from the internal twins of the martensite. *In situ* experiments in the $<121>_{LD}$ has demonstrated the nucleation, growth, and accumulation of martensite in the microstructure. The parallelism between interfacial dislocations and the internal twin of the martensite is clear. Additionally, dislocation loops seem to be left behind in the matrix after unloading and martensite needles nucleate on these dislocation loops during subsequent loading. However, it is still uncertain whether these dislocations are formed during loading or unloading. To uncover this, martensite nucleation and shrinkage was observed from the orthogonal viewing direction to $[11\bar{1}]$i.e. $[\bar{1}21]$ which corresponds to $[11\bar{1}]_{LD}$. These results are presented in the next section.

3.2. *NiTi* $[11\bar{1}]_{LD}$*and* $[\bar{1}21]$*zone axis*

In situ tensile samples were extracted along the $[11\bar{1}]_{LD}$corresponding to a $[\bar{1}21]$zone axis. The stress-displacement curve for cycle 1 is presented in Fig. 6 (supplementary video 4). As shown in the inset this sample had 11.5 % variant 1 and 3.5 % variant 2. The load-displacement curve exhibits a typical superelastic behavior; however, the maximum strain reached was only around 1.77 % compared to 5.2 % in the previous $[\bar{1}21]_{LD}$. This suggests that the transformation strains are much smaller in the $[11\bar{1}]_{LD}$. As depicted in the TEM snapshot presented in Fig. 6c, martensite nucleates from the tip of precipitate variant 1 at 650 MPa load. At the peak load of 827 MPa, at least 3 habit plane variants have nucleated and grown. The internal twin structure of one of these variants was clearly discernable (Fig. 6d). Upon unloading, the internal twins shrink, leading to reverse movement of the A-M interface (Fig. 6e). As unloading proceeds, these internal twins convert to parallel dislocations in the B2 matrix (Fig. 6f). The SADP taken from this region

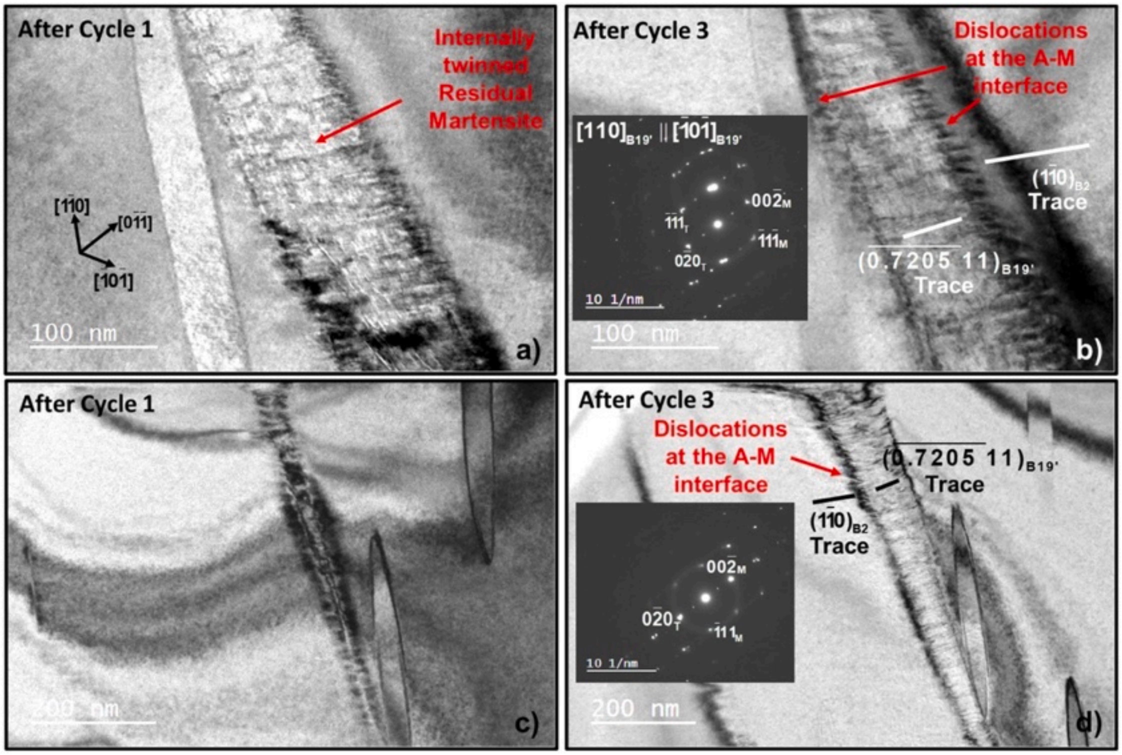

Fig. 5. Comparison between residual martensite domains after cycle 1 and cycle 3.TEM micrograph of residual martensite taken from region 1 in Fig. 2g after a) 1 and b) 3 cycles. TEM micrograph of residual martensite taken from region 2 in Fig. 2g after c) 1 and d) 3 cycles. The diffraction patterns shown in b) and d) denote type II internal twinning of martensite.

showed no signs of residual martensite, thereby confirming that these were, in fact, parallel dislocations. Additionally, it was clearly demonstrated that these dislocations are emitted into the matrix during unloading. During cycle 2, *in situ* video focusing on the parallel dislocations are presented in Fig. 7 (supplementary video 5). Upon loading, the parallel dislocations seem to transform into twinning dislocations of the martensite around 300 MPa which is less than half the transformation stress of the virgin sample. This is primarily due to the reduction in the nucleation barrier and the exact microstructural mechanism was elucidated for the first time. As the applied displacement was increased, multiple habit plane variants nucleated, and the sample catastrophically failed from a notch at 780 MPa preventing the observation of unloading behavior. The type II internal twins of the residual martensite can be clearly seen in Fig. 7e. This experiment confirms that transformation induced dislocations in the austenite matrix are emitted during unloading where the twinning dislocations transmit across the A-M interface and become sessile dislocations in the B2 matrix which may or may not pin the A-M interface. However, precipitate deformation was not observed in either of the loading orientations presented until now but was observed in *ex situ* TEM analysis of bulk samples fatigued along the $<011>_{LD}$ [21]. To uncover the mechanism behind that observation, samples with $[10\bar{1}]_{LD}$and $[0\bar{1}0]$zone axis were subjected to *in situ* TEM deformation. These results are presented in the next section.

3.3. *NiTi* $[10\bar{1}]_{LD}$*and* $[0\bar{1}0]$*zone axis*

In these tests, the maximum applied displacement was incremented from 100 nm to 225 nm to precisely capture the initiation of precipitate deformation. A total of 30 cycles were applied, and surprisingly, for the first time, we observed the reversible transformation of Ni_4Ti_3 precipitates from cycle 10, 175 nm applied displacement (4 % strain) up to cycle 29, 225 nm applied displacement (5.5 % strain). The precipitates were observed to sustain up to 4 % local strains and transformed at around 1100 MPa. The applied strain was also completely reversible. In fact, strain recovery was near 100 % for all the cycles in this loading orientation. To further probe the transformation of precipitates, a one-of-a kind experiment was attempted for the first time to our knowledge. In cycle 28, instead of recording the bright field image, the selected area diffraction pattern was recorded. The rate of deformation and the maximum applied displacement were kept the same as in cycle 27. By aligning the time stamps of the diffraction pattern and the bright field video, we could precisely capture the diffraction signatures of the transforming precipitate. During the transformation of precipitates, new diffraction spots (Fig. 8g) appear and become brighter as the volume fraction of the transformed phase increases to accommodate more strain. These diffraction spots gradually disappear during unloading, suggesting complete recovery (Fig. 8h, i) (see supplementary videos 6 and 7). The unloaded microstructure shows no signs of residual martensite nor any residual deformation inside precipitates for all the loading cycles (Fig. 8j). However, we suspect that this is not the case in bulk samples. In our previous study on $<110>_{LD}$ bulk samples fatigued under compression for over 20 cycles showed clear signs of deformation of precipitates (Fig. 8c) [21].

The trace of the residual deformation in Fig. 8c exactly matches the trace of the transformed phase inside the precipitates in Fig. 8g, suggesting that precipitate transformation could be prevalent in bulk samples but may not be completely reversible. As the applied deformation was increased from 175 nm to 225 nm, the precipitates accommodated 1.9 % to 4 % reversible strains locally. More precipitates began to reversibly transform as the applied displacement was increased.

4. Discussion

4.1. *Superelasticity in the nanoscale: effect of loading orientation*

This study has demonstrated superelasticity of 100 nm single crys-

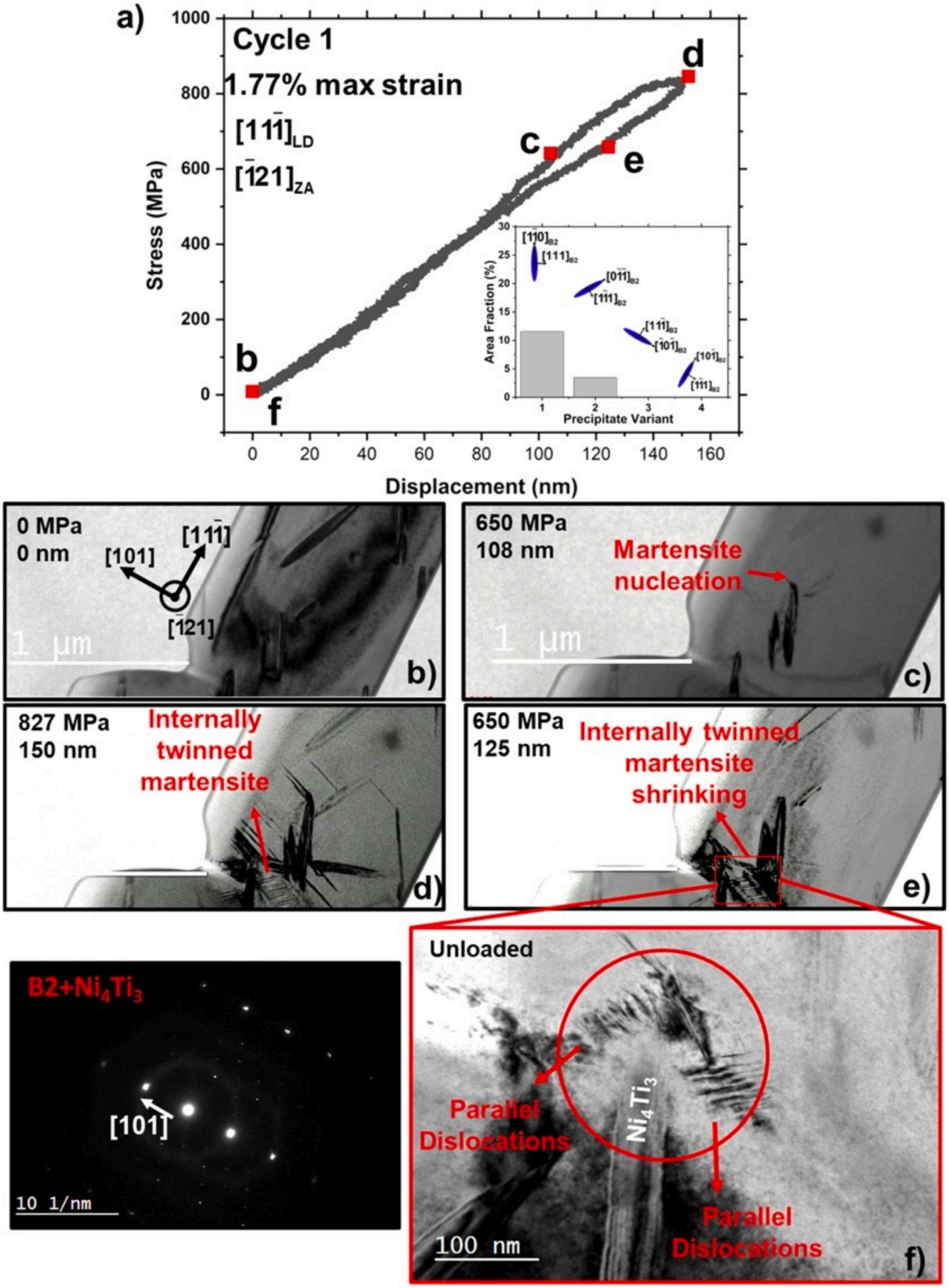

Fig. 6. a) Stress displacement curve and TEM snapshots for the $[11\overline{1}]_{LD}$ sample. b) Sample before loading. c) Martensite nucleates from the tip of precipitate variant 1. D) Internal twins of a martensite variant are clearly visible at the peak load. e) Internally twinned martensite shrinking during unloading. f) Dislocations parallel to the internal twins of the martensite were left behind after unloading. The SADP shows no signs of residual martensite in these locations. See supplementary video 4.

talline samples pulled along ⟨111⟩, ⟨121⟩, and ⟨101⟩ loading orientations. Among all the orientations, $[10\overline{1}]_{LD}$exhibited the maximum strain accommodation of up to 5.5 %, recovered about 5.3 %, and transformation stress of 520 MPa. On the other hand, the $[11\overline{1}]_{LD}$exhibited the least strain accommodation of 1.77 %, recovered about 1.7 %, and the highest transformation stress of 650 MPa. Whereas $[\overline{1}21]_{LD}$ accommodated up to 5.2 % strain, recovered only 4.1 %, and exhibited transformation stress of 480 MPa. An earlier study reported that recoverability and transformation stresses were orientation independent in the nanopillars [44]; however, that was clearly not the case in this study. According to theoretical calculations by [55] rooted in the phenomenological theory of martensitic transformation (PTMC), the

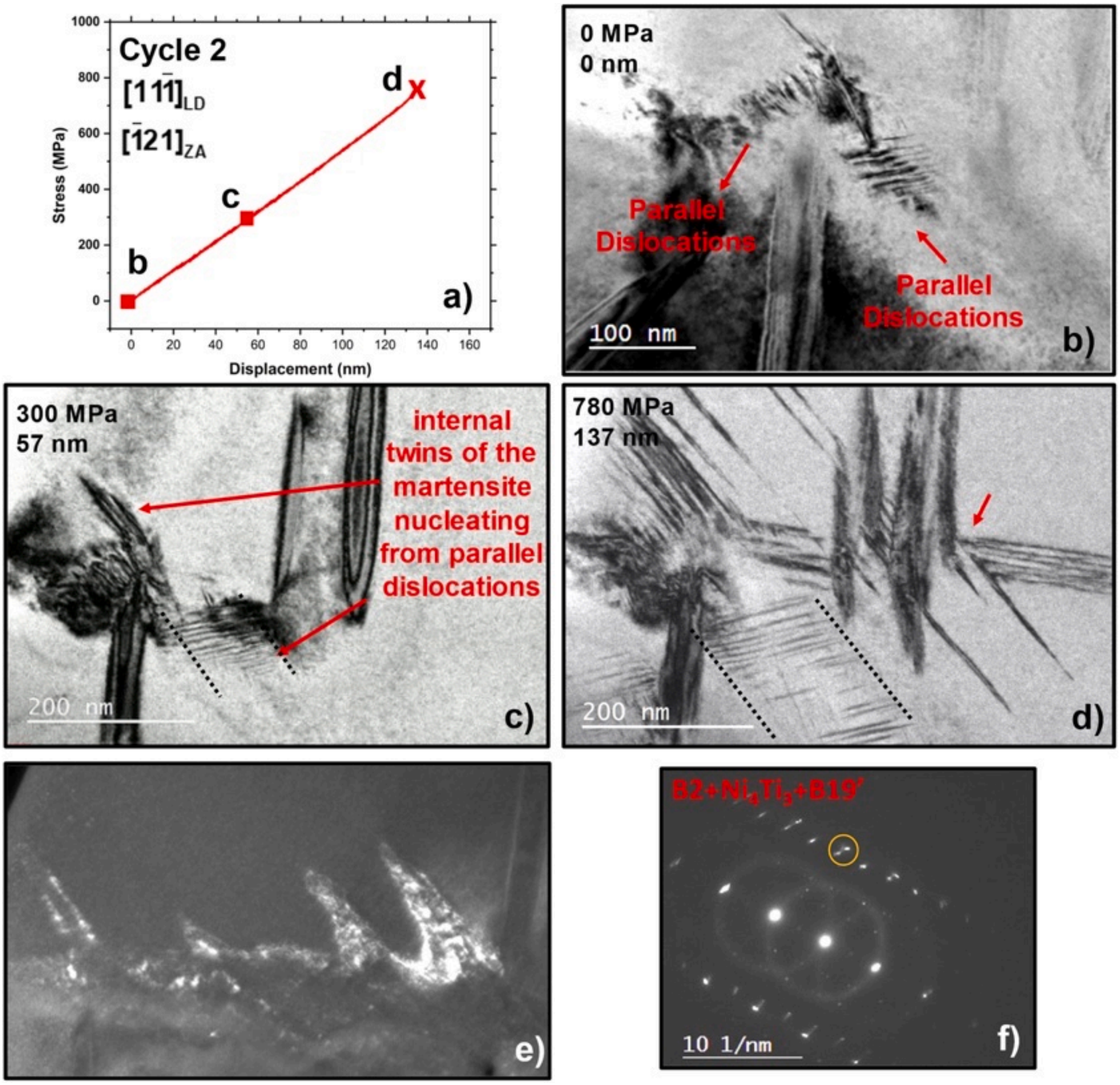

Fig. 7. a) Cycle 2 loading curve for $[11\bar{1}]_{LD}$ sample. b) TEM micrograph before loading. c) At a stress of 300 MPa, parallel dislocations become the internal twin of the martensite. d) TEM snapshot taken just before failure shows that the internal twins have widened, and the martensite has grown. The red arrow shows the nucleation of a martensite HPV from the interface of another HPV. e) Dark field image of residual martensite after failure, internal twinning clearly visible. Notice the parallelism between the internal twins and the dislocations shown in b). f) Diffraction pattern of residual martensite. See supplementary video 5.

$\langle 121\rangle_{LD}$, before detwinning, is supposed to exhibit around 6.4 %, $\langle 111\rangle_{LD}$ around 6 % and $\langle 101\rangle_{LD}$ around 5.3 % recoverable strains, suggesting that only the $\langle 101\rangle_{LD}$ nano samples exhibit strains close to theory. The theory assumes the most observed type II twinning mode in the martensite, which was also observed in this study, to make the calculations. Additionally, the volume fraction distribution of different precipitate variants could significantly influence the selection of martensite habit plane variants (HPV) and transformation stress levels [56,57] as stress-induced martensite always nucleates from precipitates. In the $\langle 111\rangle_{LD,}$ which had the least recoverable strains of 1.7 %, at least four HPVs were observed to nucleate and grow. However, only 20 % of the matrix transformed. This sample had an 11.5 % volume fraction of variant 1 and 3.5% of variant 2. Whereas the sample with the highest recoverability, $\langle 101\rangle_{LD}$, had 21 % variant 4, 2.6 % variant 3, and nucleated only 1 HPVs. In this case, more than 95 % of the matrix and some precipitates transformed. This suggests that habit plane variant selection due to the interaction between the applied stress and stress field of the precipitate plays a role in recoverable strains and transformation stress. Precipitates aligned parallel to the loading direction are the most conducive for superelasticity as evidenced from $\langle 101\rangle_{LD}$. Moreover, all the studies reporting calculations of theoretical transformation strains assume the non-transformation of precipitates. However, the experimental results presented here suggest that theoretical limits are reached only when the precipitates transform. The precipitates were observed to transform only in the $\langle 101\rangle_{LD}$ when the precipitates' longitudinal axis was parallel to the loading direction, suggesting that its relative orientation highly influences the maximum achievable reversible strain during loading. Moreover, the actual recoverability upon unloading is also influenced by the relative orientation of precipitates as will be discussed in Section 4.3.

4.2. *Nucleation and growth of martensite*

Consistently, it was observed that martensite nucleates from Ni_4Ti_3 precipitate interface and tips. Precipitates aid in martensite nucleation as (i) introducing Ni-rich precipitates starve the surrounding austenite matrix of nickel, which increases the martensite start temperature (M_s) locally and promotes transformation at a lower stress [58] (ii) the coherent precipitates generate an internal stress field that interacts with the external stress and preferentially nucleates specific martensitic variants [56,57] influencing the maximum achievable transformation strains. In the $\langle 121\rangle_{LD}$, the nucleation embryo of martensite was less

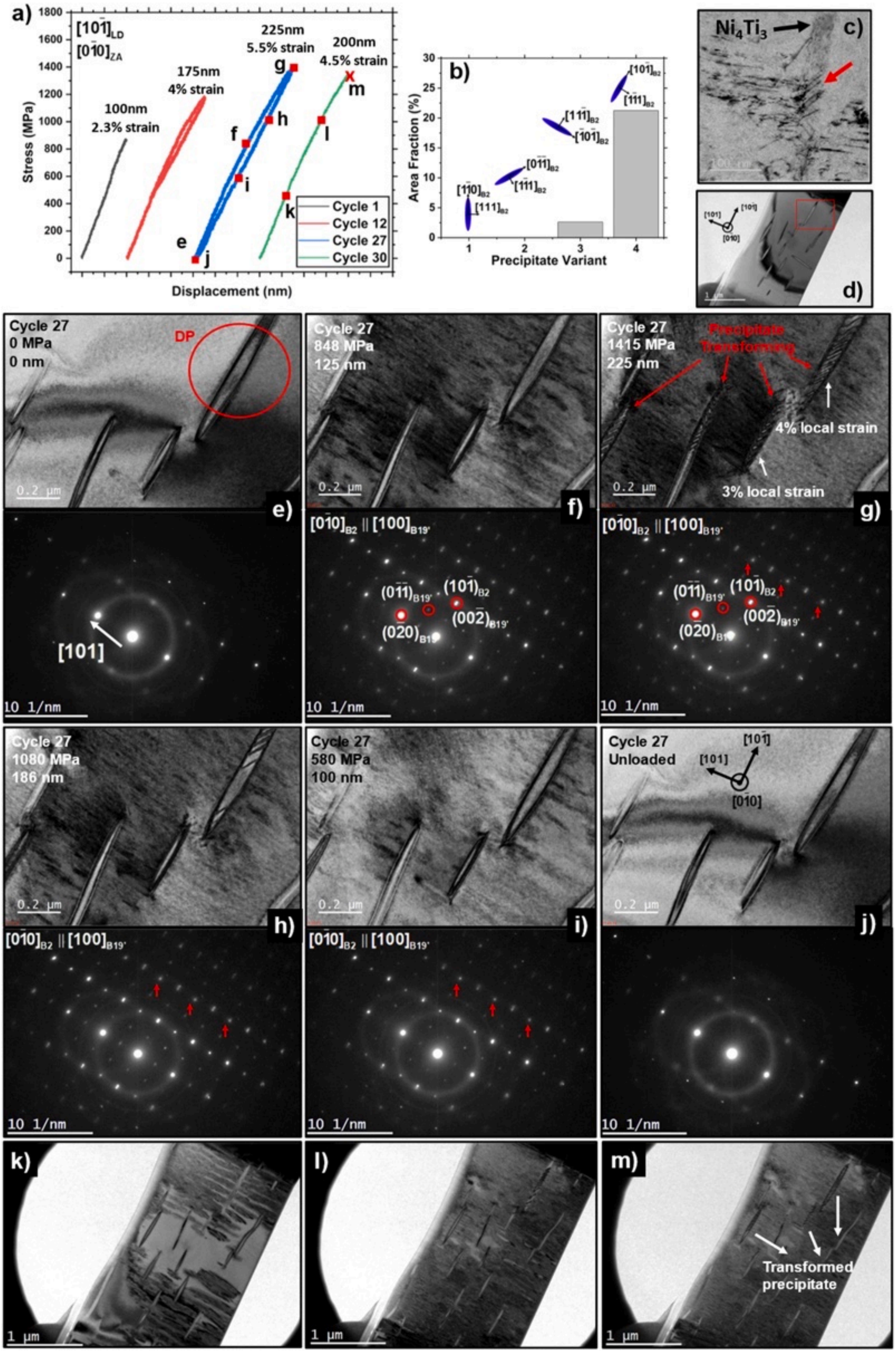

Fig. 8. a) Stress-Displacement curve of $[10\bar{1}]_{LD}$for cycles 1, 12, 27 and 30. b) Area fraction of different precipitate variants. c) TEM micrograph showing deformation of precipitates in <110>$_{LD}$ bulk samples cycled 20 times in compression [21]. Red arrows point out the deformation morphology inside the precipitate. d) TEM micrograph of *in situ* sample. Redbox denotes the region of interest for real-time observation. e)–j) snapshots of the TEM bright field video and the SADP video taken during cycle 27 and 28 respectively. The rate of deformation and the maximum applied displacement was the same for these cycles. Red arrows in the DP in figures g)–i) point out the diffraction spots corresponding to the transformed phase inside the precipitate k) to m) Low magnification TEM snapshots take during cycle 30. Only 1 martensite variant is present and multiple precipitates can be seen transforming. See supplementary videos 6 and 7.

than 10 nm wide. When these plates grow to about 25 nm wide, coalescence with other martensite plates occurred (Figs. 3d and 4d). After coalescence, martensite detwinning occurred (Figs. 3e and 4e). Upon unloading, martensite needles revert to their point of nucleation; however, detwinned martensite does not revert. A previous study on thermally induced martensite reports the smallest martensite nuclei consist of two internally twinned HPVs connected by a type I twin junction plane [54,59] and proposes that the type I junction plane nucleates prior to the HPV. However, the observations of stress-induced martensite in this study suggest that the individual HPVs can nucleate and be stable without self-accommodation. The junction plane is formed later, when multiple HPVs interact at higher applied strains as shown in Fig. 4e and inset of Fig. 4f. In $<121>_{LD}$ and $<101>_{LD}$, after nucleation, martensite needles grow longitudinally and coalesce. The needles de-coalesce and shrink longitudinally upon unloading in the nanoscale. The formulation of growth kinetics of thermoelastic martensite rooted in thermodynamics predicts that martensite, modeled as an oblate spheroid, prefers to grow radially i.e. longitudinally [60] as observed in this study.

In the $<111>_{LD}$, multiple martensitic variants were nucleated. Again, the point of nucleation was precipitate. In addition to that, as the applied displacement was increased, martensite plates suddenly nucleated from other plates (red arrow in Fig. 7d). This is a consequence of the self-accommodation and interface autocatalysis [61]. The interfacial dislocations help nucleate other HPVs. In bulk cases, self-accommodated martensite may nucleate instantaneously [59,62] probably due to the triaxial stress state; however, in the nano-samples in the plane stress condition, single HPVs first nucleate, then as these grow, other variants can nucleate from this interface via autocatalysis to aid in interface strain accommodation and/or form type I twin junction planes when intersecting with other HPVs.

4.3. Transformation induced defects

In $<121>_{LD}$, transformation-induced defects consisted of dislocation loops and residual martensite. Detwinned martensite did not recover upon unloading. Parallel dislocations at the austenite-martensite interface pinned the interface, making it sessile. During detwinning, it is possible that the twinning dislocations pile-up at the austenite-martensite interface, causing stress concentration. During unloading, as the austenite-martensite interface reverts, the stress concentration is relaxed by allowing the piled-up twinning dislocations to transmit into the austenite matrix as parallel dislocations on the closest austenite slip system with the maximum resolved shear stress. As the critical resolved shear stress to move dislocations in austenite is much larger than the transformation stress, these dislocations become sessile and pin the interface. An early mechanism of twinning dislocation pile-up along the A-M interface that triggers a dislocation reaction and subsequent emission of slip dislocations into the austenite matrix during unloading was proposed by Kajiwara [22,24]. The energetics of this dislocation reaction has also been elucidated by molecular dynamics simulations before [33]. However, in this study the twinning dislocation seems to be directly transmitting across the A-M interface into the austenite matrix. Moreover, a recent study by Akamine et al. [63] has clearly shown that the dislocations do not exist along the internal twin boundary of the martensite during thermal cycling and martensite yield stress is much higher than the transformation stress [64]. Therefore, it can be concluded that the transformation induced parallel dislocations are emitted into the austenite matrix only during unloading. Additionally, upon close observation of Fig. 5b and d the dislocations at the interface appear as a direct extension of the internal twins. In addition to interfacial dislocations, parallel dislocation loops were also found to be pinned by the stress field ahead of a residual martensite tip (Figs. 3g and 4f). These dislocation loops lie on parallel $\{011\}_{B2}$slip planes with $<100>_{B2}$ burgers vector. Figs. 6 and 7 clearly show that the internal twins transform into parallel dislocations during unloading, and in the subsequent cycles, these dislocation loops and parallel dislocations become the twinning dislocations in the martensite as shown (Figs. 3,4, 6, and 7). As these individual twin variants of martensite grow wider, longer and coalesce with other martensite needles, detwinning begins. Detwinning occurs inhomogeneously, only in regions with a high density of martensite needles, such as near precipitates (Fig. 9a and 9b). However, once detwinning commences, these precipitates act as obstacles to it. Fig. 9c shows that the parallel interfacial dislocations get pinned at the precipitate interface. Moreover, after three cycles, distortion of internal twins in the region between the two precipitates is evident. Even the interfacial dislocations are distorted similarly (two red arrows in Fig. 9d). Martensite pinning by precipitates was observed in our previous study [51] and elongated dislocation loops were observed to be pinned at precipitate interfaces in fatigued bulk single crystals [21]. These observations clearly suggest that precipitates aid forward transformation but restrict reverse transformation. In $<101>_{LD}$, martensite was pinned only by the tips of precipitate variant 4. This suggests that the relative orientation of the precipitate variant with respect to the loading direction and the HPV influences the nature of pinning. Hence, one can conclude that precipitates not only influence variant selection during loading but also influence variant pinning upon unloading.

4.4. Transformation of Ni_4Ti_3 precipitates

For the first time, reversible transformation of Ni_4Ti_3 precipitate was observed. The lattice constants $a_R = 6.704$ Å and $\alpha_R = 113.85^\circ$ [78] were used for simulated Ni_4Ti_3 diffraction pattern, conforming to the experimental pattern within 1.16 % agreement. The diffraction patterns for transformed phase (marked by green arrows in Fig. 10a) were matched to R-phase using trigonal cell with lattice parameters a=7.38 Å c=5.32 Å α=90° β=90° γ=120° within an error of 2.4 %. It is known that the ageing conditions and the consequent precipitate morphology significantly influences the formation of the R-phase, however the precipitates themselves were never observed to transform [65]. However, historic *in situ* TEM studies only looked at thermally induced phase transformations. The morphology of R-phase in the precipitate observed in this study closely resembles the one that appears in the austenite matrix in [65]. The thermodynamic mechanism behind the precipitate transformation is unknown and out of scope of current investigation. Furthermore, this new finding opens an avenue for tailoring the microstructure of NiTi SMAs to achieve superior superelasticity in the nanoscale via directional precipitation. These precipitates seem to undergo reversible transformations even in bulk samples as shown in Fig. 8c.

4.5. Implications of the results for advanced understanding and modeling of shape memory materials

4.5.1. Reduction of transformation stress and increase in hardening with cycling

It is well known that under superelasticity conditions, the transformation stress decreases with cycles [66,67], which is also noted in our results. The cause of such a decrease has not been well understood. The generation of internal defects, such as dislocations, will create favorable stress fields that assist the nucleation of martensite in subsequent cycles (Figs. 3 and 4). In this study, we noted the formation of dislocation loops are emitted to the matrix upon reverse motion of the martensite. This is consistent with recent theories [33]. There are multiple loops that are parallel, as observed in this work, and their density evolves with cycling. We also draw attention to the formation of residual martensite (Fig. 9), which could also alter the stress-strain response. The unique results in this study point to the reduction in measured transformation stresses due to the precipitate fields and also due to the presence of transformation-induced dislocations. The reduction of martensite transformation stress is nearly 150 MPa due to precipitates and almost 350 MPa due to the presence of residual dislocations. In

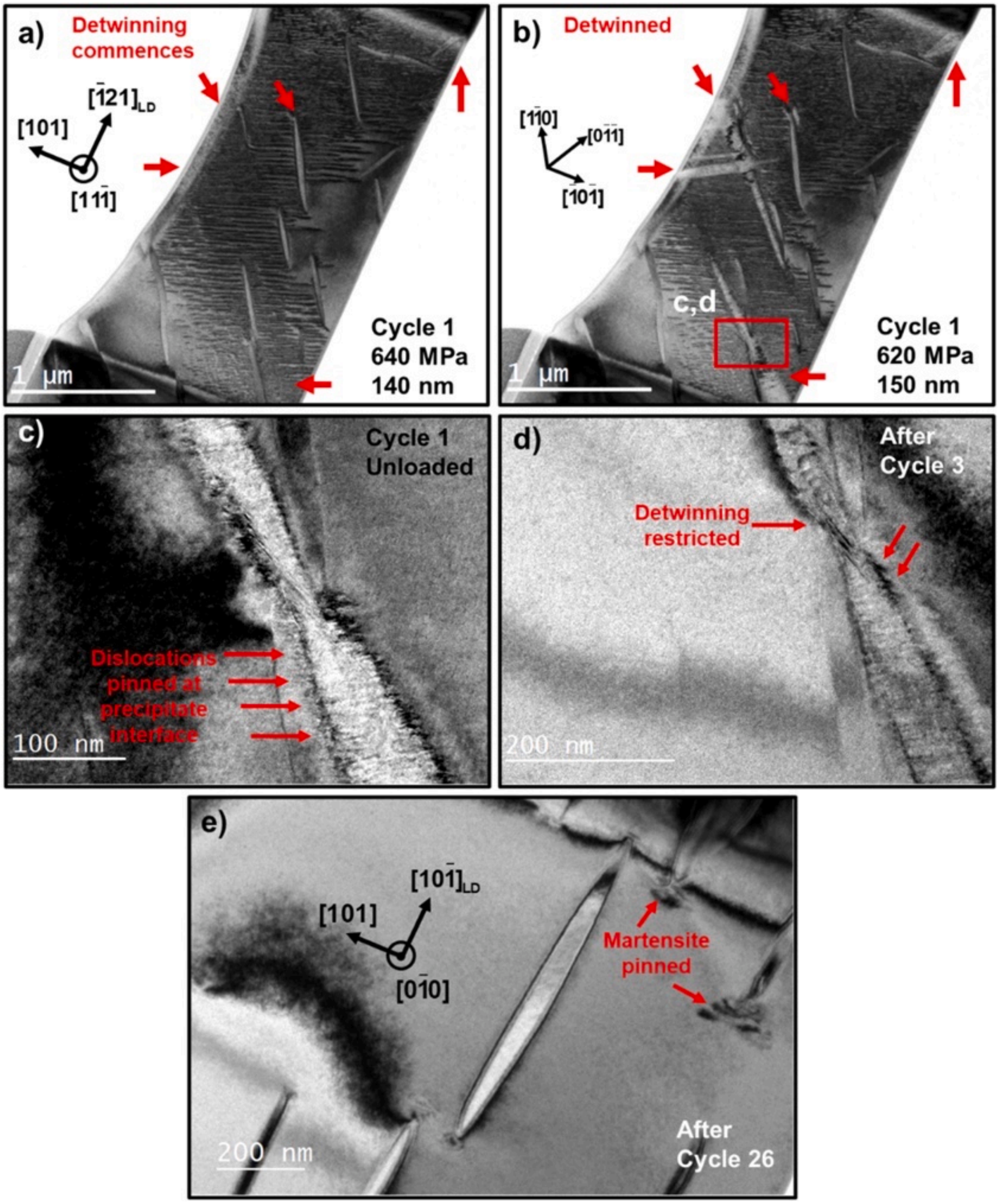

Fig. 9. a) Detwinning commences in regions near precipitates with a high density of martensite needles (red arrows). b) Detwinning clearly visible (red arrows). c) During reverse transformation, interfacial dislocations get pinned at the precipitate interface (red arrows). d) Since the precipitates restrict detwinning, the distortion of the internal twins has magnified. e) Martensite pinned at tips of precipitates in the $<101>_{LD}$.

combination, these magnitudes can lower the intrinsic transformation stress considerably and by as much as 500 MPa, upon cycling. Therefore, the *in-situ* TEM experiments provide unique insights into the reduction of transformation stress upon cycling.

4.5.2. *The source of dislocation slip in shape memory alloys*

An early mechanism was proposed [24] that showed selected slip systems were activated in the austenite phase. The deformation of the martensite is primarily by twinning, and the observed slip in austenite coincided with the martensite twin plane and direction [27,68,69]. Therefore, the twin boundaries in martensite are postulated to be the source of the dislocation slip in shape memory alloys [28,33] based on experimental observations and theory. The current *in-situ* TEM results provide direct evidence of this hypothesis by matching the plane traces in martensite that transform into austenite dislocation bands. The spacing of these dislocations on the twin plane has been calculated previously. They exhibit a finite separation (in the range of 5 to 30 nm) obtained from consideration of anisotropic elastic energy and twin boundary energies [70,71]. The width of the transformation-induced parallel dislocation segments and dislocation loops were of the same order in this study.

4.5.3. *The location of slip emission in the cycle*

Recent simulations showed that the slip emission occurs during the

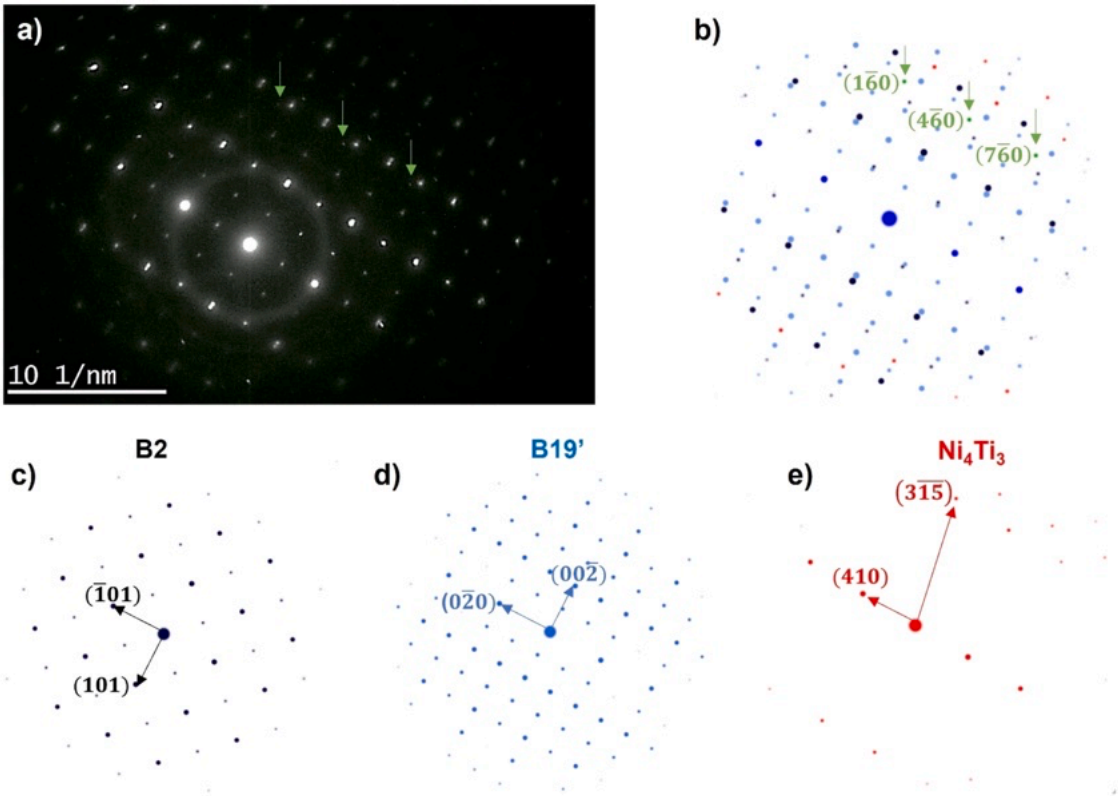

Fig. 10. a) Experimental diffraction pattern at 225 nm displacement where green arrows show spots which cannot be identified with B2, Ni_4Ti_3 or B19'. b) Simulated diffraction which is formed by overlapping. c) B2 → $[0\bar{1}0]$ zone d) B19' → [100] zone and e) Ni_4Ti_3 → $[\overline{0.34}\ 1.35\ \overline{0.45}]$ zone. The spots shown with green arrow were matched with R phase by comparing both the ratio of interplanar spacing and angle between spots within an error of 2.4 %.

unloading portion of the cycle [33]. The current experiments confirm this finding. As the martensite front recedes, the dislocation motion could encounter a higher barrier in austenite, resulting in the emission of a stacking fault. We note that the theoretical modeling confirmed the precise levels at which such emission occurs. Upon examination of Fig. 6 (e), (f), we can pinpoint the occurrence of the slip between points e and f. When the slip emission occurs during unloading, the result would be that there would be an imbalance in the forward and reverse flow behavior, resulting in a modification of the stress hysteresis. This observation is consistent with earlier experimental observations [66,67, 72].

4.5.4. Accumulation of plastic strains with cycling

The generation of dislocations in the martensitic phase has been concluded in previous studies. It was inferred from experiments on NiTi dating back to 1986 [66] and more recently theoretically [33,70,71]. The emission of dislocations is progressive and results in the accumulation of irrecoverable strains. This observation has been confirmed in early studies on bulk specimens [67,73,74] and unambiguously shown in this work. Residual martensite domains accumulate and thicken with cycling (Fig. 5). These events result in a reduction of the transformation strain component because of the lack of volume that can undergo transformation. We also make the observation that fully detwinned martensite does not fully recover (Fig. 2(g)), which is an intriguing finding worthy of further work.

4.5.5. Detwinning of martensite

The martensite is internally twinned and exhibits two variants in the stressed state, as shown in many previous works [64,75–77]. Transformation strains encompass contributions from martensite formation and detwinning and are highly crystal orientation dependent. The detwinning of the martensite contributes to additional strains [55] and it has been observed in our experiments (Figs. 2(e), 3(e) and 4(d)). It is known detwinning results in strains that exceed the correspondent variant pair formation. This work shows that it is facilitated by martensite-precipitate interactions (Fig. 9). The current work illustrates the emergence of detwinned zones where intersections have occurred. Higher levels of internal stresses generated at these intersections could cause potential fatigue damage in these materials.

4.5.6. The role of precipitates

The precipitates are confirmed to facilitate transformation as shown in previous atomistic simulations [78,79] and confirmed in this work as well. The volume fraction of the precipitates is nearly 15 % in this alloy; in fact, it has been shown that the solutionized NiTi exhibits slightly higher transformation strains compared to the aged cases. The main effect of the precipitates is that it affects the transformation stress, the selection of the martensite variant and in case of slip, and the precise slip system [80]. Early studies determined the internal stress fields using micromechanical concepts [81,82] and later studies with molecular dynamics [78,79] were also fruitful. In this study, it was further uncovered that the precipitates pinned the martensite and restricted detwinning, which could translate to modifying interaction energy terms in the thermomechanical models [25,83–85].

4.5.7. Implications on hysteresis

All the factors outlined above point to the development of dislocations from interfaces and the interaction of these dislocations with precipitates. The magnitude of the elastic strain is reduced during reversed transformation, corresponding to a lower twin-disconnection density compared to the forward strain case [10]. This imbalance between dislocation densities during forward and reverse strains results in a dislocation surplus. Consequently, the law of conversation of Burger's vectors requires an excess of dislocations to be produced on a cycle-by-cycle basis. Such emission of slip creates an evolution of dislocation density that traverses to the austenite domains, preventing the material from returning to the initial state. Also, the emission of dislocations produces non-closure of the hysteresis loop, which accumulates on a cycle-by-cycle basis as observed in the experiments [25]. Regarding hysteresis, the reverse flow is governed by the extent of slip upon unloading. Then, the reverse transformation and the transformation induced slip behavior, both with their unique critical stresses, govern the hysteresis. Hence, the level of hysteresis is expected to be strongly maximum strain dependent [86] and cannot be assumed as a constant as adopted in early studies.

4.5.8. Transformation stresses and their modification

Overall, the magnitude of transformation stresses in this study agrees with the theory of transformation stress proposed earlier by Sehitoglu et al. [87], which is based on energy minimization and accounts for interfacial defects. This theory predicted strong crystal orientation dependence with extreme values in CRSS for $\langle 011\rangle$ and $\langle 111\rangle$ orientations. Specifically, CRSS levels of 380 MPa and 225 MPa were theoretically predicted corresponding for [011] and [111] orientations, respectively (Table 1 in [87]). The Schmid factors for these two orientations were approximately 0.4. Similarly, in the current experiments, the $\langle 011\rangle$ orientation resulted in higher transformation stresses compared to $\langle 111\rangle$ by a factor of 1.5. Further, we note that the current results in this paper show strong agreement with previous bulk specimen experimental results [88,89] published earlier from the Illinois group.

5. Conclusions

The aim of the current work was to demonstrate tensile superelasticity and study the fatigue behavior of NiTi shape memory alloy in the 100 nm regime relevant for many nanoscale applications. Additionally, by observing the deformation in real time, several key mechanisms regarding fatigue irreversibility and the role of precipitates were uncovered. Significant contributions of this study are as follows.

1. NiTi samples with thicknesses of the order of 85 to 100 nm were shown to exhibit superelastic recoverability in three different loading orientations. The $<121>_{LD}$ sustained tensile stress up to 640 MPa and recovered up to 4.1 % strain, $<111>_{LD}$ sustained 800 MPa and recovered 1.7 % strain, and $<110>_{LD}$ sustained up to 1.4 GPa and recovered 5.3 % strain.
2. Martensite needles preferred to grow longitudinally, coalesce and detwin only at local stress hotspots in the microstructure. Single internally twinned HPVs with type II twins were the smallest observable nucleation unit, and Type I twin junction formed between intersecting HPVs during loading.
3. During loading, the relative orientation of the precipitates with respect to the tensile direction significantly influenced martensite variant selection and acted as obstacles to martensite detwinning. During unloading, precipitates restricted martensite shrinkage by pinning the interfacial dislocations and, consequently, influenced the magnitude of reversible strains. Based on the precipitate orientation, a preference was observed between precipitate tips and interfaces for pinning HPVs.
4. Dislocations parallel to the internal twin of the martensite were observed to form along the austenite-martensite interface. During unloading, the twinning dislocations of the martensite transmit across the austenite-martensite interface and become sessile dislocations on the closest austenite slip system. In addition to interfacial dislocations, parallel dislocation loops were also observed to form during unloading. Martensite nucleated from these dislocations during re-loading.
5. For the first time, in the $<101>_{LD,}$ precipitates oriented along the loading direction were observed to transform to R-phase at stresses $>$1 GPa and accommodated up to 4 % reversible strain for over 20 cycles. Reversible phase transformation of precipitates may be occurring in bulk samples as well.

CRediT authorship contribution statement

R. Sidharth: Writing – original draft, Visualization, Data curation, Conceptualization. **T.B. Celebi:** Writing – review & editing, Visualization, Data curation. **H. Sehitoglu:** Writing – review & editing, Supervision, Funding acquisition.

Declaration of competing interest

The authors declare that they have no known competing financial interests or personal relationships that could have appeared to influence the work reported in this paper.

Acknowledgments

The work is supported by the National Science Foundation, NSF-DMR 2104971. The experiments were carried out in part in the Materials Research Laboratory, Central Research Facilities, University of Illinois. Prof. M. Nishida of Kyushu University is gratefully acknowledged in discussions of the R-phase.

Supplementary materials

Supplementary material associated with this article can be found, in the online version, at doi:10.1016/j.actamat.2024.119990.

Appendix

To clearly delineate defects like dislocations and residual martensite in the bright field images in Figs. 3–5, and 9, we imaged the *in situ* samples after tilting (note that only single tilt is allowed in the PI95 Picoindenter, so all the diffraction conditions were not accessible). Some of these images are shown in Fig. A1. Please compare images before and after tilting. The red arrows point out dislocation visibility/invisibility upon tilting. Due to residual contrast and local bending, at least partial or even complete defect invisibility was observed. The residual martensite domain and dislocations can be clearly distinguished.

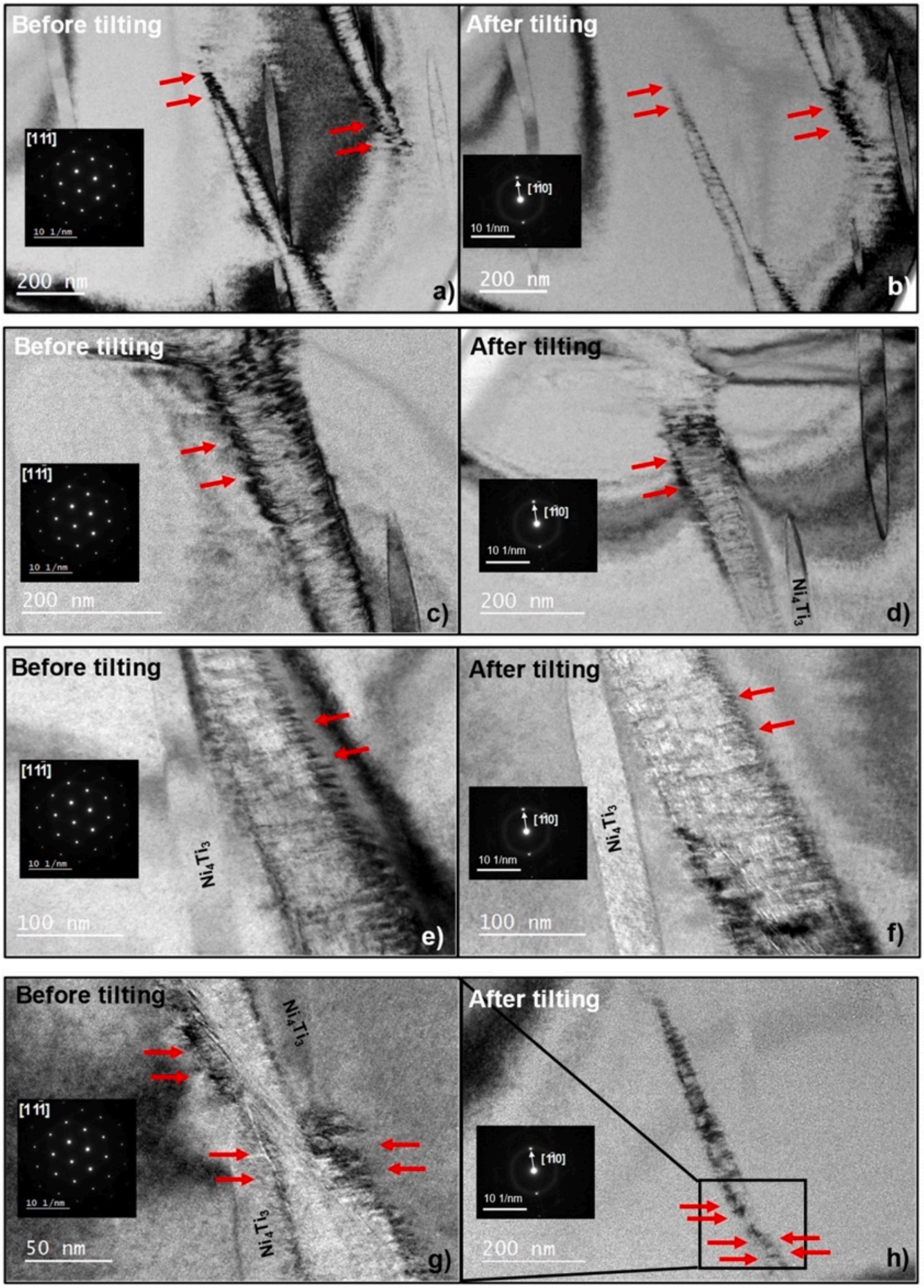

Fig. A1. Dislocation contrast can be clearly seen in a), c), e), g) and partial or complete dislocation invisibility was achieved after tilting the sample as seen in b), d), f) and h).

Snapshots taken from supplementary video 2 capturing detwinning are shown in Fig. A2.

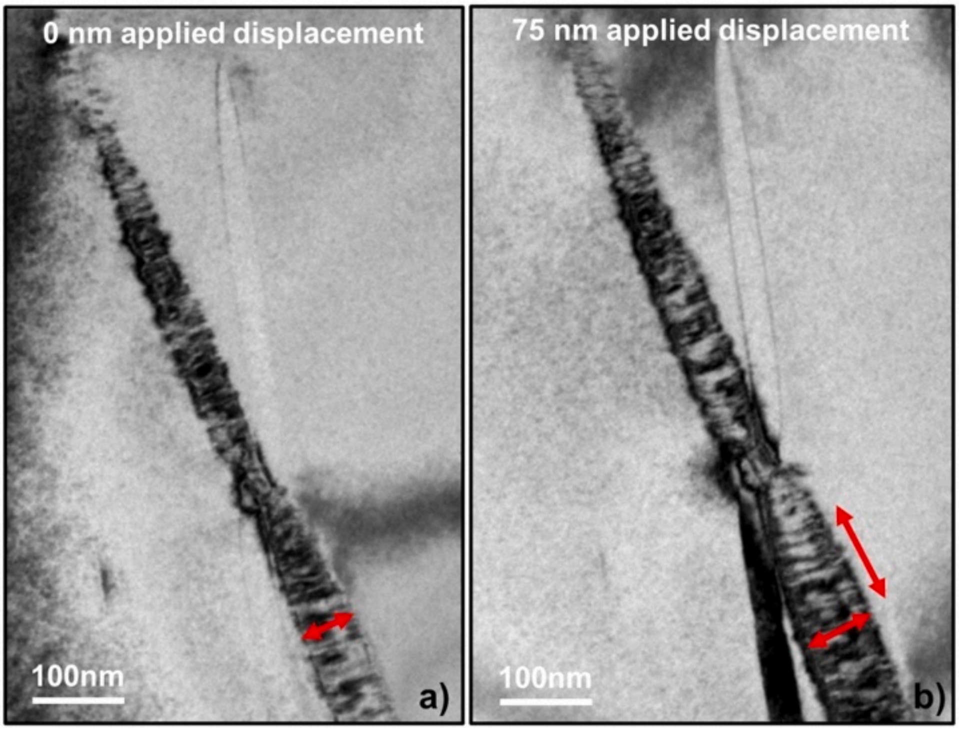

Fig. A2. Residual martensite and the internal twins have visibly widened when compared between a) 0 nm and b) 75 nm applied displacement. The diffraction contrast of the internal twins can be clearly seen in the bright field images.

The lattice constants $a_R = 6.704$ Å and $\alpha_R = 113.85^\circ$ [78] were used for simulated Ni_4Ti_3 diffraction pattern, conforming to the experimental pattern within 1.16 % agreement. The blue circles are diffraction spots obtained from the precipitate in our experiments in Fig. A3a and the simulated diffraction spots are shown in Fig. A3b.

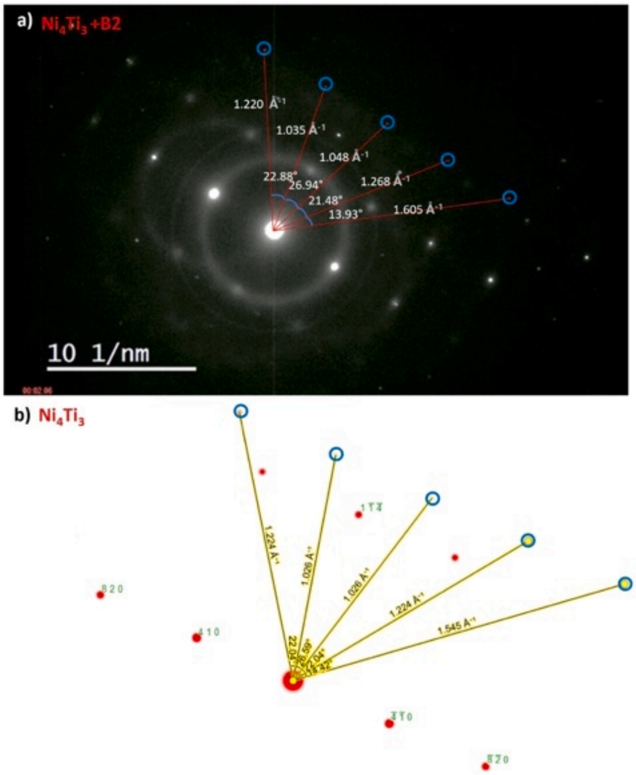

Fig. A3. a) Experimental diffraction pattern at zero applied load. Both diffracted spots from B2 and Ni4Ti3 are visible. Angles and distances between the spots diffracted from Ni4Ti3 are shown. b) Simulated diffraction pattern for Ni4Ti3. Same angles and distances with the experimental pattern are shown. Experimental diffraction pattern and simulated diffraction pattern are matched with an error of 1.16 percent comparing both distances and angles between spots.

References

[1] K. Otsuka, C.M. Wayman, Shape Memory Materials, Cambridge University Press, 1999.

[2] C. Wayman, The growth of martensite since EC Bain (1924)-some milestones, Mater. Sci. Forum 56 (1990) 1–32. Trans Tech Publ.

[3] G. Olson, H. Hartman, Martensite and life: displacive transformations as biological processes, J. Phys. Colloq. 43 (C4) (1982) 855–865.

[4] D.C. Lagoudas, Shape Memory Alloys: Modeling and Engineering Applications, Springer, 2008.

[5] D.J. Hartl, D.C. Lagoudas, Aerospace applications of shape memory alloys, Proc. Inst. Mech. Eng. Part G J. Aerosp. Eng. 221 (4) (2007) 535–552.

[6] D. Safranski, K. Dupont, K. Gall, Pseudoelastic NiTiNOL in orthopaedic applications, Shape Mem. Superelast. 6 (3) (2020) 332–341.

[7] T.W. Duerig, The use of superelasticity in modern medicine, MRS Bull. 27 (2) (2002) 101–104.

[8] E.A. Williams, G. Shaw, M. Elahinia, Control of an automotive shape memory alloy mirror actuator, Mechatronics 20 (5) (2010) 527–534.

[9] J.V. Humbeeck, S. Kustov, Active and passive damping of noise and vibrations through shape memory alloys: applications and mechanisms, Smart Mater. Struct. 14 (5) (2005) S171–S185.

[10] H. Sehitoglu, G. Anlas, A.S.K. Mohammed, Shape memory alloys–frontier developments, in: M.H.F. Aliabadi, W.O. Soboyejo (Eds.). Comprehensive Structural Integrity, 2nd ed., Elsevier, Oxford, 2023, pp. 610–679.

[11] K. Bhattacharya, R.D. James, The material is the machine, Science 307 (5706) (2005) 53–54.

[12] Y. Fu, H. Du, W. Huang, S. Zhang, M. Hu, TiNi-based thin films in MEMS applications: a review, Sens. Actuators A Phys. 112 (2–3) (2004) 395–408.

[13] R.H. Wolf, A.H. Heuer, TiNi (shape memory) films silicon for MEMS applications, J. Microelectromech. Syst. 4 (4) (1995) 206–212.

[14] M. Kohl, Shape Memory Microactuators, Springer Science & Business Media, 2004.

[15] S.A. Wilson, R.P. Jourdain, Q. Zhang, R.A. Dorey, C.R. Bowen, M. Willander, Q. U. Wahab, S.M. Al-Hilli, O. Nur, E. Quandt, New materials for micro-scale sensors and actuators: an engineering review, Mater. Sci. Eng. R Rep. 56 (1–6) (2007) 1–129.

[16] C.R. Knick, D.J. Sharar, A.A. Wilson, G.L. Smith, C.J. Morris, H.A. Bruck, High frequency, low power, electrically actuated shape memory alloy MEMS bimorph thermal actuators, J. Micromech. Microeng. 29 (7) (2019) 075005.

[17] Y.Q. Fu, J. Luo, A. Flewitt, S.E. Ong, S. Zhang, H. Du, W. Milne, Microactuators of free-standing TiNiCu films, Smart Mater. Struct. 16 (6) (2007) 2651.

[18] D.J. Laser, J.G. Santiago, A review of micropumps, J. Micromech. Microeng. 14 (6) (2004) R35.

[19] E. Makino, T. Mitsuya, T. Shibata, Fabrication of TiNi shape memory micropump, Sens. Actuators A Phys. 88 (3) (2001) 256–262.

[20] P. Krulevitch, A.P. Lee, P.B. Ramsey, J.C. Trevino, J. Hamilton, M.A. Northrup, Thin film shape memory alloy microactuators, J. Microelectromech. Syst. 5 (4) (1996) 270–282.

[21] R. Sidharth, A. Mohammed, H. Sehitoglu, Functional fatigue of NiTi shape memory alloy: effect of loading frequency and source of residual strains, Shape Mem. Superelast. 8 (2022) 1–19.

[22] S. Kajiwara, Characteristic features of shape memory effect and related transformation behavior in Fe-based alloys, Mater. Sci. Eng. A 273-275 (1999) 67–88.

[23] S. Kajiwara, T. Kikuchi, Reversible movement of the austenite-martensite interface and dislocation structures in reverse-transformed austenite in Fe-Ni-C alloys, Philos. Mag. A 48 (4) (1983) 509–526.

[24] S. Kajiwara, T. Kikuchi, Dislocation structures produced by reverse martensitic transformation in a Cu-Zn alloy, Acta Metall. 30 (2) (1982) 589–598.

[25] R.F. Hamilton, H. Sehitoglu, Y. Chumlyakov, H. Maier, Stress dependence of the hysteresis in single crystal NiTi alloys, Acta Mater. 52 (11) (2004) 3383–3402.

[26] D. Roy, V. Buravalla, P. Mangalgiri, S. Allegavi, U. Ramamurty, Mechanical characterization of NiTi SMA wires using a dynamic mechanical analyzer, Mater. Sci. Eng. A 494 (1–2) (2008) 429–435.

[27] D. Norfleet, P. Sarosi, S. Manchiraju, M.X. Wagner, M. Uchic, P. Anderson, M. Mills, Transformation-induced plasticity during pseudoelastic deformation in Ni–Ti microcrystals, Acta Mater. 57 (12) (2009) 3549–3561.

[28] A. Pelton, G. Huang, P. Moine, R. Sinclair, Effects of thermal cycling on microstructure and properties in Nitinol, Mater. Sci. Eng. A 532 (2012) 130–138.

[29] M. Bowers, X. Chen, M. De Graef, P.M. Anderson, M. Mills, Characterization and modeling of defects generated in pseudoelastically deformed NiTi microcrystals, Scr. Mater. 78 (2014) 69–72.

[30] T. Simon, A. Kröger, C. Somsen, A. Dlouhy, G. Eggeler, On the multiplication of dislocations during martensitic transformations in NiTi shape memory alloys, Acta Mater. 58 (5) (2010) 1850–1860.

[31] R. Delville, B. Malard, J. Pilch, P. Sittner, D. Schryvers, Transmission electron microscopy investigation of dislocation slip during superelastic cycling of Ni–Ti wires, Int. J. Plast. 27 (2) (2011) 282–297.

[32] A. Ibarra, J. San Juan, E. Bocanegra, M. Nó, Evolution of microstructure and thermomechanical properties during superelastic compression cycling in Cu–Al–Ni single crystals, Acta Mater. 55 (14) (2007) 4789–4798.

[33] A.S.K. Mohammed, H. Sehitoglu, Martensitic twin boundary migration as a source of irreversible slip in shape memory alloys, Acta Mater. 186 (2020) 50–67.

[34] H.M. Paranjape, S. Manchiraju, P.M. Anderson, A phase field–Finite element approach to model the interaction between phase transformations and plasticity in shape memory alloys, Int. J. Plast. 80 (2016) 1–18.

[35] H.M. Paranjape, M.L. Bowers, M.J. Mills, P.M. Anderson, Mechanisms for phase transformation induced slip in shape memory alloy micro-crystals, Acta Mater. 132 (2017) 444–454.

[36] M. Sade, R. Rapacioli, M. Ahlers, Fatigue in Cu-Zn-Al single crystals, Acta Metall. 33 (3) (1985) 487–497.

[37] C. Damiani, M. Sade, F. Lovey, Fatigue in Cu-Zn-Al single crystals during pseudoelastic cycling: *in situ* observations by SEM and optical microscopy, J. Phys. IV 112 (2003) 623–626 (Proceedings), EDP sciences.

[38] Y. Wu, J. Yaacoub, F. Brenne, W. Abuzaid, D. Canadinc, H. Sehitoglu, Deshielding effects on fatigue crack growth in shape memory alloys-a study on CuZnAl single-crystalline materials, Acta Mater. 176 (2019) 155–166.

[39] K. Otsuka, X. Ren, Physical metallurgy of Ti–Ni-based shape memory alloys, Prog. Mater. Sci. 50 (5) (2005) 511–678.

[40] J.S. Juan, M.L. Nó, C.A. Schuh, Nanoscale shape-memory alloys for ultrahigh mechanical damping, Nat. Nanotechnol. 4 (7) (2009) 415–419.

[41] J. San Juan, M. Nó, C. Schuh, Superelastic cycling of Cu–Al–Ni shape memory alloy micropillars, Acta Mater. 60 (10) (2012) 4093–4106.

[42] B.G. Clark, D.S. Gianola, O. Kraft, C.P. Frick, Size independent shape memory behavior of nickel–titanium, Adv. Eng. Mater. 12 (8) (2010) 808–815.

[43] C. Frick, S. Orso, E. Arzt, Loss of pseudoelasticity in nickel–titanium sub-micron compression pillars, Acta Mater. 55 (11) (2007) 3845–3855.

[44] C.P. Frick, B.G. Clark, S. Orso, P. Sonnweber-Ribic, E. Arzt, Orientation-independent pseudoelasticity in small-scale NiTi compression pillars, Scr. Mater. 59 (1) (2008) 7–10.

[45] J. Ye, R.K. Mishra, A.R. Pelton, A.M. Minor, Direct observation of the NiTi martensitic phase transformation in nanoscale volumes, Acta Mater. 58 (2) (2010) 490–498.

[46] W. Tirry, D. Schryvers, *In situ* transmission electron microscopy of stress-induced martensite with focus on martensite twinning, Mater. Sci. Eng. A 481 (2008) 420–425.

[47] X. Jiang, M. Hida, Y. Takemoto, A. Sakakibara, H. Yasuda, H. Mori, *In situ* observation of stress-induced martensitic transformation and plastic deformation in TiNi alloy, Mater. Sci. Eng. A 238 (2) (1997) 303–308.

[48] A. Kröger, S. Dziaszyk, J. Frenzel, C. Somsen, A. Dlouhy, G. Eggeler, Direct transmission electron microscopy observations of martensitic transformations in Ni-rich NiTi single crystals during *in situ* cooling and straining, Mater. Sci. Eng. A 481 (2008) 452–456.

[49] A. Kröger, R. Wernhardt, C. Somsen, G. Eggeler, A. Wieck, *In situ* transmission electron microscopy-investigations on the strain-induced B19′-phase in NiTi shape memory alloys structured by focused ion beam, Mater. Sci. Eng. A 438 (2006) 513–516.

[50] S. Manchiraju, A. Kroeger, C. Somsen, A. Dlouhy, G. Eggeler, P. Sarosi, P. Anderson, M. Mills, Pseudoelastic deformation and size effects during *in situ* transmission electron microscopy tensile testing of NiTi, Acta Mater. 60 (6–7) (2012) 2770–2777.

[51] R. Sidharth, J. Stinville, H. Sehitoglu, Fatigue and fracture of shape memory alloys in the nanoscale: an *in-situ* TEM study, Scr. Mater. 234 (2023) 115577.

[52] J. Stinville, E.R. Yao, P.G. Callahan, J. Shin, F. Wang, M.P. Echlin, T.M. Pollock, D. S. Gianola, Dislocation dynamics in a nickel-based superalloy via *in-situ* transmission scanning electron microscopy, Acta Mater. 168 (2019) 152–166.

[53] J.W. Christian, S. Mahajan, Deformation twinning, Prog. Mater. Sci. 39 (1–2) (1995) 1–157.

[54] M. Nishida, T. Nishiura, H. Kawano, T. Inamura, Self-accommodation of B19′ martensite in Ti–Ni shape memory alloys–Part I. Morphological and crystallographic studies of the variant selection rule, Philos. Mag. 92 (17) (2012) 2215–2233.

[55] H. Sehitoglu, R. Hamilton, D. Canadinc, X. Zhang, Detwinning in NiTi alloys, Metall. Mater. Trans. 34 (1) (2003) 5.

[56] K. Gall, H. Sehitoglu, Y.I. Chumlyakov, I.V. Kireeva, H.J. Maier, The influence of aging on critical transformation stress levels and martensite start temperatures in NiTi: part I–aged microstructure and micro-mechanical modeling, (1999).

[57] K. Gall, H. Sehitoglu, Y.I. Chumlyakov, I.V. Kireeva, H.J. Maier, The influence of aging on critical transformation stress levels and martensite start temperatures in NiTi: part II–discussion of experimental results, (1999).

[58] L. Bataillard, J.E. Bidaux, R. Gotthardt, Interaction between microstructure and multiple-step transformation in binary NiTi alloys using *in-situ* transmission electron microscopy observations, Philos. Mag. A 78 (2) (1998) 327–344.

[59] Y. Soejima, S. Motomura, M. Mitsuhara, T. Inamura, M. Nishida, *In situ* scanning electron microscopy study of the thermoelastic martensitic transformation in Ti–Ni shape memory alloy, Acta Mater. 103 (2016) 352–360.

[60] V. Raghavan, M. Cohen, Growth path of a martensitic particle, Acta Metall. 20 (6) (1972) 779–786.

[61] G. Olson, M. Cohen, A perspective on martensitic nucleation, Annu. Rev. Mater. Sci. 11 (1) (1981) 1–32.

[62] B.K. Ravari, S. Farjami, M. Nishida, Effects of Ni concentration and aging conditions on multistage martensitic transformation in aged Ni-rich Ti–Ni alloys, Acta Mater. 69 (2014) 17–29.

[63] H. Akamine, A. Heima, Y. Soejima, M. Mitsuhara, T. Inamura, M. Nishida, Where and when are dislocations induced by thermal cycling in Ti–Ni shape memory alloys? Acta Mater. 244 (2023) 118588.

[64] H. Sehitoglu, I. Karaman, R. Anderson, X. Zhang, K. Gall, H. Maier, Y. Chumlyakov, Compressive response of NiTi single crystals, Acta Mater. 48 (13) (2000) 3311–3326.

[65] J. Michutta, C. Somsen, A. Yawny, A. Dlouhy, G. Eggeler, Elementary martensitic transformation processes in Ni-rich NiTi single crystals with Ni4Ti3 precipitates, Acta Mater. 54 (13) (2006) 3525–3542.

[66] S. Miyazaki, T. Imai, Y. Igo, K. Otsuka, Effect of cyclic deformation on the pseudoelasticity characteristics of Ti-Ni alloys, Metall. Trans. A 17 (1) (1986) 115–120.

[67] H. Sehitoglu, R. Anderson, I. Karaman, K. Gall, Y. Chumlyakov, Cyclic deformation behavior of single crystal NiTi, Mater. Sci. Eng. A 314 (1) (2001) 67–74.

[68] T. Simon, A. Kroger, C. Somsen, A. Dlouhy, G. Eggeler, On the multiplication of dislocations during martensitic transformations in NiTi shape memory alloys, Acta Mater. 58 (2010) 1850–1860 (Copyright 2010, The Institution of Engineering and Technology).

[69] J. Zhang, C. Somsen, T. Simon, X. Ding, S. Hou, S. Ren, X. Ren, G. Eggeler, K. Otsuka, J. Sun, Leaf-like dislocation substructures and the decrease of martensitic start temperatures: a new explanation for functional fatigue during thermally induced martensitic transformations in coarse-grained Ni-rich Ti–Ni shape memory alloys, Acta Mater. 60 (5) (2012) 1999–2006.

[70] A.S.K. Mohammed, H. Sehitoglu, Modeling the interface structure of type II twin boundary in B19′ NiTi from an atomistic and topological standpoint, Acta Mater. 183 (2020) 93–109.

[71] A.S.K. Mohammed, H. Sehitoglu, Strain-sensitive topological evolution of twin interfaces, Acta Mater. 208 (2021) 116716.

[72] L. Heller, H. Seiner, P. Šittner, P. Sedlák, O. Tyc, L. Kadeřávek, On the plastic deformation accompanying cyclic martensitic transformation in thermomechanically loaded NiTi, Int. J. Plast. 111 (2018) 53–71.

[73] A.M. David, C.L. Dimitris, Thermomechanical characterization of NiTiCu and NiTi SMA actuators: influence of plastic strains, Smart Mater. Struct. 9 (5) (2000) 640.

[74] P. Sedmák, P. Šittner, J. Pilch, C. Curfs, Instability of cyclic superelastic deformation of NiTi investigated by synchrotron X-ray diffraction, Acta Mater. 94 (2015) 257–270.

[75] K. Gall, H. Sehitoglu, Y.I. Chumlyakov, I. Kireeva, Tension–compression asymmetry of the stress–strain response in aged single crystal and polycrystalline NiTi, Acta Mater. 47 (4) (1999) 1203–1217.

[76] H. Sehitoglu, J. Jun, X. Zhang, I. Karaman, Y. Chumlyakov, H.J. Maier, K. Gall, Shape memory and pseudoelastic behavior of 51.5% Ni–Ti single crystals in solutionized and overaged state, Acta Mater. 49 (17) (2001) 3609–3620.

[77] H. Sehitoglu, X. Zhang, Y. Chumlyakov, I. Karaman, K. Gall, H. Maier, Observations on stress-induced transformations in NiTi alloys, in: Proceedings of the IUTAM Symposium on Mechanics of Martensitic Phase Transformation in Solids, Springer, Dordrecht, 2002, pp. 103–109.

[78] P. Chowdhury, L. Patriarca, G. Ren, H. Sehitoglu, Molecular dynamics modeling of NiTi superelasticity in presence of nanoprecipitates, Int. J. Plast. 81 (2016) 152–167.

[79] P. Chowdhury, G. Ren, H. Sehitoglu, NiTi superelasticity via atomistic simulations, Philos. Mag. Lett. 95 (12) (2015) 574–586.

[80] T. Ezaz, J. Wang, H. Sehitoglu, H. Maier, Plastic deformation of NiTi shape memory alloys, Acta Mater. 61 (1) (2013) 67–78.

[81] K. Gall, H. Sehitoglu, Y.I. Chumlyakov, I.V. Kireeva, H.J. Maier, The influence on critical transformation stress levels and martensite start temperatures in NiTi: part I-aged microstructure and micro-mechanical modeling, ASME J. Eng. Mater. Technol. 121 (1) (1999) 19–27.

[82] K. Gall, H. Sehitoglu, Y. Chumlyakov, I.V. Kireeva, H.J. Maier, The influence of aging on critical transformation stress levels and martensite start temperatures in NiTi: part II–discussion of experimental results, Trans. ASME 121 (1999) 28–37.

[83] R. Sidharth, A. Mohammed, W. Abuzaid, H. Sehitoglu, Unraveling frequency effects in shape memory alloys: NiTi and FeMnAlNi. Shape Memory and Superelasticity, Springer, 2021, pp. 1–15.

[84] M. Huang, L.C. Brinson, A Multivariant model for single crystal shape memory alloy behavior, J. Mech. Phys. Solids 46 (8) (1998) 1379–1409.

[85] K. Gall, H. Sehitoglu, The role of texture in tension–compression asymmetry in polycrystalline NiTi, Int. J. Plast. 15 (1) (1999) 69–92.

[86] K. Gall, H. Sehitoglu, Y.I. Chumlyakov, I.V. Kireeva, Pseudoelastic cyclic stress-strain response of over-aged single crystal Ti-50.8at%Ni, Scr. Mater. 40 (1) (1998) 7–12.

[87] S. Alkan, H. Sehitoglu, Prediction of transformation stresses in NiTi shape memory alloy, Acta Mater. 175 (2019) 182–195.

[88] R. Sidharth, A.S.K. Mohammed, W. Abuzaid, H. Sehitoglu, Unraveling frequency effects in shape memory alloys: NiTi and FeMnAlNi, Shape Mem. Superelast. 7 (2) (2021) 235–249.

[89] G.J. Pataky, E. Ertekin, H. Sehitoglu, Elastocaloric cooling potential of NiTi, Ni2FeGa, and CoNiAl, Acta Mater. 96 (2015) 420–427.